Impact of high-order effects on the dynamics of localized states in the Swift-Hohenberg equation

Bachelor thesis

submitted by
Justus Johannes Keussen

Supervisor:
apl. Prof. Dr. Svetlana Gurevich

Co-Supervisor:
Prof. Dr. Julien Javaloyes

institut für theoretische physik

Universität Münster

Contents

Chapter 1

Introduction

The Swift-Hohenberg equation (SHE) is a widely studied nonlinear partial differential equation known for its ability to model pattern formation in various physical systems. Originally, the SHE was introduced to describe thermal convection in fluid layers [1], the SHE has since found applications in fields ranging from nonlinear optics to reaction-diffusion systems [2]. The equation is notable for describing periodic patterns, which manifest as regularly repeating structures like stripes or hexagons. In addition to periodic patterns, the SHE captures the dynamics of localized states, which are spatially confined structures that can persist over time. These localized states are of particular interest due to their relevance in understanding complex systems and their potential applications in technology. For instance, they are crucial in explaining the formation of convective cells in thermal systems [1, 3] and the emergence of localized structures in reaction-diffusion systems and optical resonators [4, 2]. Additionally, localized states provide insights into bistable and multistable phenomena, as seen e.g., in hydrodynamic systems [5].

Localized states in the SHE exhibit a rich variety of dynamics, including the phenomenon of homoclinic snaking, where solutions form a sequence of connected branches, that snake back and forth in parameter space [4]. This intricate structure is sensitive to various factors, including dispersion effects. Dispersion, which describes the dependence of physical quantities such as the growth rate on frequency, plays a crucial role in the dynamics of localized states. While the impact of second-order effects like diffusion or dispersion (d_2) has already been studied [6], higher-order dispersion effects, such as

third-order (d_3) and fourth-order (d_4) dispersion, remain less explored.
This thesis aims to fill this gap by investigating the influence of high-order effects on the dynamics of localized states in the SHE. We focus on how high-order terms modify the homoclinic snaking structures and the formation of isolated branches, so-called isolas. By systematically varying the dispersion parameters and examining their interplay with the control parameter y_0, which in optical systems describes the deviation of the amplitude of the injected field.
The study starts with an overview of the properties of the Swift-Hohenberg Equation (SHE) and the mathematical framework used to analyze localized states. The effects of third-order dispersion are then examined, highlighting how it leads to the breaking of homoclinic snaking and the emergence of isolas. By considering d_3 as linearly dependent on the injection amplitude y_0, the conditions under which isolas reconnect and form intertwined branches are identified. The impact of fourth-order dispersion is also analyzed, demonstrating its significant influence on periodic branches and the expansion of the pinning region. The linear dependence of d_4 on y_0 is investigated to understand the formation of multiple snaking structures and their merging into overlapping isolas.
Additionally, the role of second-order contribution is explored with emphasis on its distinct effects on periodic branches and snaking structures. By varying d_2 and considering its linear dependence on y_0, a detailed exploration of the phase space is conducted, identifying transcritical bifurcations and their influence on the dynamics of localized states. The results illustrate the complex interplay between different dispersion orders and their significant impact on the behavior of the SHE.
In conclusion, this thesis contributes to the understanding of high-order dispersion effects in the SHE, offering new perspectives on the dynamics of localized states. The findings have potential applications in various fields, including nonlinear optics and fluid dynamics, where the control of localized structures is crucial. Future research directions are proposed to further explore the intriguing phenomena uncovered in this study, paving the way for advancements in the theoretical and practical understanding of pattern formation in complex systems.

Chapter 2

Theoretical background

This chapter explains the theoretical preliminaries and numerical methods used in this thesis.

2.1 Nonlinear dynamical systems

Nonlinear dynamical systems play an important role in many fields of science and technology. Unlike linear systems, nonlinear systems exhibit more complex behavior that is often difficult to predict. These systems can generate phenomena such as bifurcations, periodic/quasi periodic oscillations and chaos [7]. A function f is considered to be linear if it satisfies the principles of superposition and homogeneity. Mathematically, this can be described by the equation:

$$f(\alpha x + \beta y) = \alpha f(x) + \beta f(y), \tag{2.1}$$

where x, y are the inputs and α and β are constants. If Eq.(2.1) is not satisfied, f is called nonlinear. In a linear system, the superposition principle allows known solutions of differential equations to be combined into new solutions. This can be used to construct general solutions from a family of linearly independent solutions. Since the superposition principle does not apply in nonlinear systems, this is not possible here, which makes finding general solutions extremely difficult.
An arbitrary dynamical system can be written as an initial value problem:

$$\dot{x} = F(x, t) \tag{2.2}$$

with $x(t_0) = x_0$, where $F(x,t)$ is a vector-valued function that describes the rate of change of the state vector x with respect to time t. In this context, x is a n-dimensional state vector:

$$x = \begin{pmatrix} x_1 \\ x_2 \\ \vdots \\ x_n \end{pmatrix},$$

and $F(x,t)$ is an n-dimensional vector field:

$$F(x,t) = \begin{pmatrix} F_1(x_1, x_2, \ldots, x_n, t) \\ F_2(x_1, x_2, \ldots, x_n, t) \\ \vdots \\ F_n(x_1, x_2, \ldots, x_n, t) \end{pmatrix}.$$

Each component $F_i(x,t)$ represents the rate of change of the corresponding state variable, x_i and can be a function of all state variables and time. The system resulting in ordinary differential equations can thus be written as:

$$\begin{aligned} \dot{x}_1 &= F_1(x_1, x_2, \ldots, x_n, t), \\ \dot{x}_2 &= F_2(x_1, x_2, \ldots, x_n, t), \\ &\vdots \\ \dot{x}_n &= F_n(x_1, x_2, \ldots, x_n, t). \end{aligned}$$

This formulation allows for the modeling of dynamical systems where the dynamics of each state variable depend on the interactions between all variables and possibly on time.

A dynamical system is considered nonlinear if at least one of the components of Eq.(2.2) is nonlinear.

If F is not explicit time t dependent, i.e.:

$$\dot{x} = F(x), \tag{2.3}$$

the system (2.3) is called autonomous. If, in contrast, it is explicit time dependent, then it is called non-autonomous. In non-autonomous systems, the dynamics can change over time due to the explicit time dependence.

This makes the analysis more complex than with an autonomous system, as the system's behavior can vary depending on the specific time at which it is observed. Non-autonomous systems are common in real-world applications where external influences or time-dependent parameters affect the system's evolution. For example, the driven harmonic oscillator:

$$m\ddot{x} + b\dot{x} + kx = F\cos(t), \tag{2.4}$$

where x is the position, m, b are constants describing mass and dumping and $F\cos(t)$ describes the driving force. To rewrite this system in the form of a non-autonomous dynamical system, we introduce new variables $x_1 = x$ and $x_2 = \dot{x}$. Then, the system (2.4) can be written as:

$$\begin{aligned}
\dot{x}_1 &= x_2 \\
\dot{x}_2 &= -\frac{k}{m}x_1 - \frac{b}{m}x_2 + \frac{F}{m}\cos(t)
\end{aligned}$$

where the second equation is non-autonomous. To rewrite the non-autonomous system in Equation (2.4) as an autonomous system, we introduce a third variable $x_3 = t$, representing time. The equations then become:

$$\begin{aligned}
\dot{x}_1 &= x_2, \\
\dot{x}_2 &= -\frac{b}{m}x_2 - \frac{k}{m}x_1 + \frac{F}{m}\cos(x_3), \\
\dot{x}_3 &= 1.
\end{aligned}$$

By embedding time as a state variable, we effectively eliminate the explicit time dependence in the original system, making the system autonomous in three variables[7].

2.2 Linear stability analysis

A point x^* at which $F(x^*, t) = 0$, so that the change in the system over time is zero, is called an equilibrium or fixed point. Fixed points can be linearly stable or unstable with respect to a small perturbation. These

points and their stability are of great interest in determining the dynamics of the system.
To analyze the stability of a fixed point x^*, we consider a small perturbation:

$$x(t) = x^* + \delta x(t).$$

If we insert this expression into the system (2.2), we get

$$\delta \dot{x} + \dot{x} = F(x^* + \delta x, t).$$

Since $F(x^*, t) = 0$, we can linearize the function F around the fixed point x^*:

$$F(x^* + \delta x, t) \approx F(x^*, t) + \left.\frac{\partial F}{\partial x}\right|_{x=x^*} \delta x.$$

This leads to:

$$\delta \dot{x} = \left.\frac{\partial F}{\partial x}\right|_{x=x^*} \delta x.$$

If we denote the Jacobian matrix of F at the point x^* by $J = \left.\frac{\partial F}{\partial x}\right|_{x=x^*}$, the result is

$$\delta \dot{x} = J \delta x.$$

If we set $\delta x(t) = \sum_i e^{\lambda_i t} \phi_i$ we get the linear eigenvalue problem:

$$\lambda_i \phi_i = J \phi_i,$$

where ϕ_i are the eigenvectors and λ_i are the corresponding eigenvalues of the Jacobian matrix J. The eigenvalues of the Jacobian matrix J determine the behavior of the perturbation $\delta x(t)$:

- If all eigenvalues of J have negative real parts, then $\delta x(t) \to 0$ for $t \to \infty$, and the fixed point x^* is stable.

- If at least one eigenvalue of J has a positive real part, then $\delta x(t)$ grows exponentially and the fixed point x^* is unstable.

With this, we can define three subspaces spanned by eigenvectors:

- the stable subspace whose corresponding
  eigenvalues λ satisfy $\mathrm{Re}(\lambda) < 0$

- the unstable subspace whose corresponding eigenvalues λ satisfy $\mathrm{Re}(\lambda) > 0$.
- the center subspace whose corresponding eigenvalues λ satisfy $\mathrm{Re}(\lambda) = 0$.

In the stable and unstable subspace, all solution converge/diverge exponentially fast to/away from the fixed point. The dynamics on the center subspace is not determined by the linearization but by higher order terms. When going beyond the linearization, the subspaces deform to the nearby manifolds [7].

2.3 Local bifurcations

Local bifurcations are qualitative changes in the behavior of a dynamics of the system (2.2) that occur when a parameter of the system is varied. In this chapter, we consider three basic types of local bifurcations: the saddle-node bifurcation, the transcritical bifurcation and the pitchfork bifurcation.

2.3.1 Saddle-node bifurcation

A saddle-node bifurcation occurs when two fixed points (one stable and one unstable) collide and annihilate each other when a parameter exceeds the critical value [7].
The normal form of an equation describing a saddle-node bifurcation is:

$$\frac{dx}{dt} = r + x^2. \tag{2.5}$$

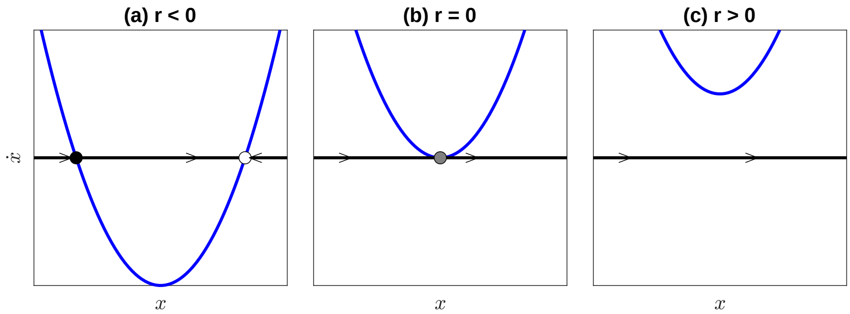

Figure 2.1: An illustration of a saddle-node bifurcation described by Eq.(2.5). When a control parameter r is varied, (a) a stable equilibrium point (filled point) and an unstable equilibrium point (unfilled circle) move toward each other, (b) and collide at the bifurcation point, (c) and then disappear. A horizontal line through the equilibrium points, with arrows showing the direction of the dynamics. The arrows illustrate the flow of solutions toward the stable equilibrium and away from the unstable equilibrium.

The dynamics of Eq.(2.5) is depicted in Fig. 2.1. Here, r is the bifurcation parameter. For $r < 0$ there are two fixed points at $x = \pm\sqrt{-r}$ one stable and one unstable, for $r = 0$ there is one fixed point (a so-called half-stable point), and for $r > 0$ there are no fixed points. Fig. 2.2 shows the corresponding bifurcation diagram, where position of fixed points are depicted as a function of r. The arrows illustrate the flow of solutions toward the stable equilibrium and away from the unstable equilibrium.

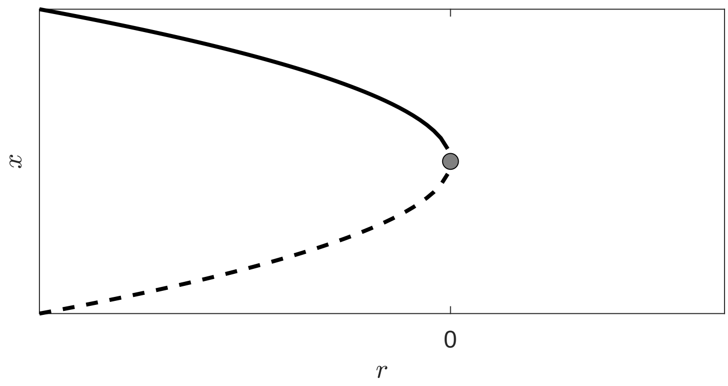

Figure 2.2: The bifurcation diagram shows the fixed points of the system (2.5) as a function of the parameter r of Fig. 2.1. For $r < 0$, there are two fixed points: one stable (solid line) and one unstable (dashed line), given by $x = \pm\sqrt{-r}$. At $r = 0$, there is a half-stable fixed point at $x = 0$ (marked by a gray dot). For $r > 0$, there are no real fixed points.

2.3.2 Transcritical bifurcation

A transcritical bifurcation occurs when two fixed points exchange their stability when a parameter exceeds the critical value [7].
The normal form of an equation describing a transcritical bifurcation is:

$$\frac{dx}{dt} = rx - x^2. \tag{2.6}$$

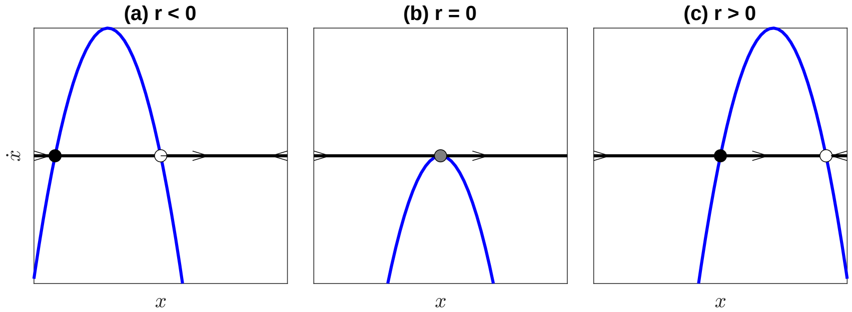

Figure 2.3: An illustration of a transcritical bifurcation, described by Eq.(2.6). When a control parameter r is varied, (a) a stable equilibrium point (filled point) and an unstable equilibrium point (unfilled circle) exist for $r < 0$, (b) they collide and exchange stability at the bifurcation point $r = 0$, (c) for $r > 0$, the stable and unstable points have exchanged their stability. A horizontal line through the equilibrium points, with arrows showing the direction of the dynamics. The arrows illustrate the flow of solutions toward the stable equilibrium and away from the unstable equilibrium.

A dynamics of Eq.(2.6) is depicted in Fig. 2.3. Here r is the bifurcation parameter. For $r < 0$, the fixed point at $x = 0$ is stable (solid line) and the fixed point at $x = r$ is unstable. For $r > 0$, the fixed point at $x = 0$ is unstable and the fixed point at $x = r$ is stable. Figure 2.4 shows the corresponding bifurcation diagram, where position of fixed points are depicted as a function of r.

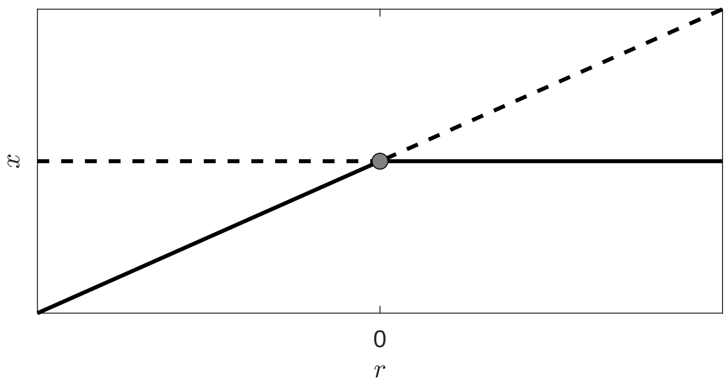

Figure 2.4: The bifurcation diagram shows the fixed points of the system (2.6) as a function of the parameter r of Fig. 2.3. For $r < 0$, there are two fixed points: one stable (solid line) at $x = r$ and one unstable (dashed line) at $x = 0$. For $r > 0$, the stability of these fixed points switches: the fixed point at $x = r$ becomes unstable (dashed line) and the fixed point at $x = 0$ becomes stable (solid line). At $r = 0$, there is a half-stable fixed point at $(0, 0)$ (marked by a gray dot).

2.3.3 Pitchfork Bifurcation

A pitchfork bifurcation occurs when a system's symmetry causes a single fixed point to split into three fixed points as a parameter is varied. This bifurcation can be classified as either supercritical or subcritical. In a supercritical pitchfork bifurcation, the system transitions from a single stable fixed point to two new stable fixed points and an intermediate unstable fixed point as the bifurcation parameter is increased. Conversely, in a subcritical pitchfork bifurcation, two unstable fixed points merge with a stable fixed point and subsequently vanish as the parameter is varied[7].
In this section, we use the example of a supercritical pitchfork bifurcation. The normal form of an equation describing this bifurcation is:

$$\frac{dx}{dt} = rx - x^3. \tag{2.7}$$

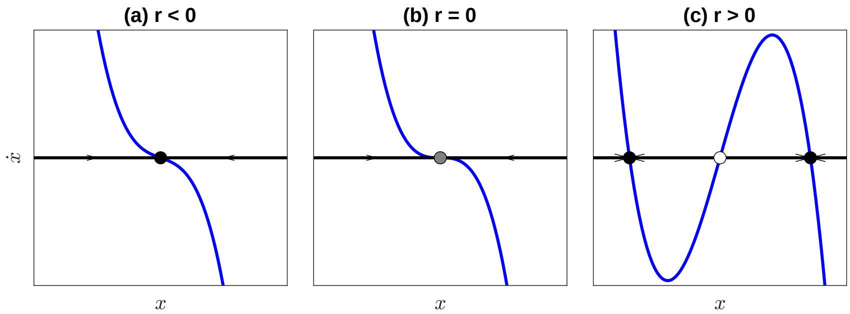

Figure 2.5: An illustration of a supercritical pitchfork bifurcation described by Eq.(2.7). When a control parameter r is varied, (a) a single stable equilibrium point (filled point) splits into three equilibrium points: one unstable (unfilled circle) and two stable (filled points), (b) at the bifurcation point. A horizontal line through the equilibrium points, with arrows showing the direction of the dynamics. The arrows illustrate the flow of solutions toward the stable equilibrium and away from the unstable equilibrium.

The dynamics of Eq.(2.7) are depicted in Fig. 2.5. Here, r is the bifurcation parameter. For $r < 0$, there is one stable fixed point at $x = 0$. For $r > 0$, the fixed point at $x = 0$ becomes unstable, and two new stable fixed points appear at $x = \pm\sqrt{r}$.

Figure 2.6 shows the corresponding bifurcation diagram, where the positions of the fixed points are depicted as a function of r.

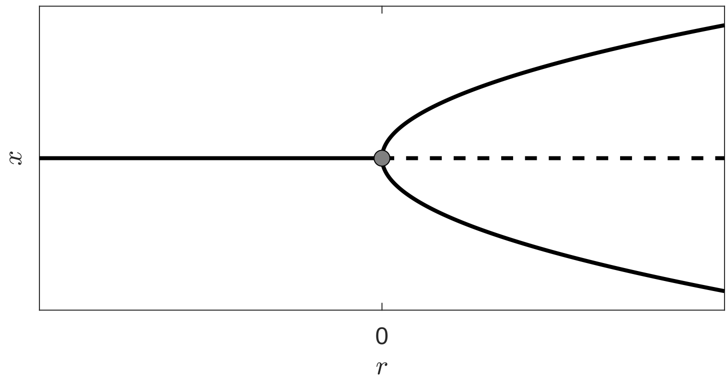

Figure 2.6: The bifurcation diagram shows the fixed points of the system (2.7) as a function of the parameter r of Fig. 2.5. For $r < 0$, there is one stable fixed point at $x = 0$ (solid line). At $r = 0$, this point becomes unstable (dashed line), and for $r > 0$, two new stable fixed points appear at $x = \pm\sqrt{r}$ (solid lines).

2.3.4 Impact of imperfections on local bifurcations

Pitchfork bifurcations often occur in symmetric systems as (2.7). In many real world problems this perfect symmetry is just an approximation an imperfection leads to a symmetry break. To investigate this, we can introduce a new parameter into the system (2.7), namely h:

$$\frac{dx}{dt} = h + rx - x^3. \tag{2.8}$$

Since h represents an imperfection, we call it the imperfection parameter [7]. For $h = 0$ we get the same bifurcation structure as in chapter 2.3.3. This is also shown in Fig. 2.7 (a). For $h \neq 0$, however, the symmetry is broken and thus the bifurcation diagram also changes. This is also demonstrated in Fig. 2.7 (b).

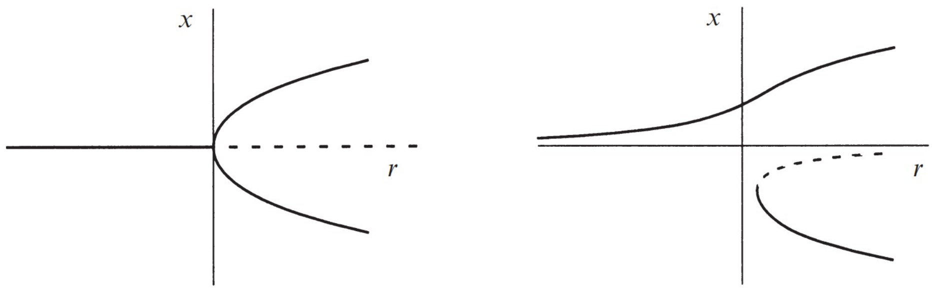

(a) $h = 0$ (b) $h \neq 0$

Figure 2.7: When $h = 0$ we have the usual pitchfork diagram (a) but when $h \neq 0$, the pitchfork disconnects into two pieces (b). The upper piece consists entirely of stable fixed points, whereas the lower piece has both stable and unstable branches. As we increase r from negative values, there's no longer a sharp transition at $r = 0$; the fixed point simply glides smoothly along the upper branch. Furthermore, the lower branch of stable points is not accessible unless we make a fairly large disturbance. This figure has been adapted from Fig. 3.6.3 of Ref. [7].

Such behavior, i.e., an abrupt change in dynamics due to a change in a parameter, can also be observed for other bifurcations. For example, a transcritical bifurcation can also react similarly to an imperfection. However, the saddle-node bifurcation is structurally stable.

2.4 Pattern Formation

Pattern formation refers to the emergence of ordered macroscopic patterns in, e.g., a physical, chemical, or biological system [3].
During the process of pattern formation, the system transitions from one homogeneous state to another, such as a periodic state. These patterns can occur both in time and in space.
In particular, this thesis focuses on spatially periodic patterns, which are also known as Turing patterns. A special emphasis in this work is placed on localized states, which are a type of pattern that plays a crucial role in this work. Localized states are spatially confined structures that arise in nonlinear systems due to the coexistence of different stable states.

Figure 2.8: Various examples of patterns in nature: Columnar Jointing at Giant's Causeway, Northern Ireland [8], Sand ripples as Turing pattern [9], Maasai giraffe cow with unique fur pattern in the Zambian savannah [10], spiral arrangement of the petals of a sunflower [11], Amphiprion ocellaris (Clown anemonefish) with color pattern in Papua New Guinea [12].

In Fig. 2.8, we can see different examples of emergent structures that can be easily found in nature. These include the hexagonal patterns in the basalt columns of the Giant's Causeway in Northern Ireland, which are formed by the slow cooling and contraction of lava [8]. We also observe ripple patterns in sand dunes, created by the interaction of wind or water with the sand [9]. The unique spot patterns on a Masai giraffe, which serve as camouflage and are an example of genetic diversity in the animal kingdom, are also depicted [10]. Additionally, the spiral arrangement of florets in a sunflower follows the Fibonacci sequence, a mathematical pattern frequently found in nature [11]. Finally, the vibrant colors and stripes of the clown anemonefish in Papua New Guinea illustrate the intricate patterns found in marine life [12].

In order to recognize how exactly a Turing pattern's emerge, we look at a spatially extended system as:

$$\dot{\phi} = L(\nabla, \nabla^2, \varepsilon)\phi + N(\phi). \tag{2.9}$$

Here, ϕ represents a field variable describing the state of the system, $L(\nabla, \nabla^2, \varepsilon)$ is a linear operator and $N(\phi)$ is the nonlinear term. Now let's take a closer look at the surroundings of the fixed point $\phi = \phi_0$ by introducing a small perturbation so that:

$$\phi = \phi_0 + \tilde{\phi}, \tag{2.10}$$

where $\tilde{\phi}$ represents a small perturbation therefore $|\tilde{\phi}| \ll 1$. We can now linearize this equation and choose the Fourier approach:

$$\tilde{\phi} \propto e^{\lambda t + ikx}, \tag{2.11}$$

where k is the wave number, which determines the spatial frequency of the perturbation and is related to the wavelength of the pattern. If we solve the resulting equation for λ, we obtain the so-called dispersion relation $\lambda(k)$.

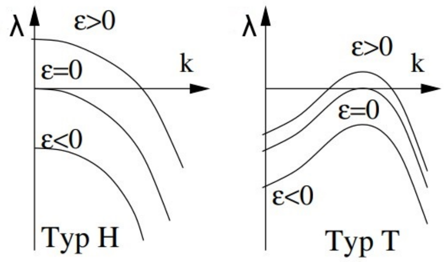

Figure 2.9: Examples of dispersion relation $\lambda(k)$ for different values of control parameter ε. On the left side, the instability is homogeneous (Typ H) because the k value with the greatest growth rate is $k = 0$. The instability on the right side results in the growth of a periodic pattern in space (Typ T) because because the k value with the greatest growth rate is $k \neq 0$. This figure has been adapted from Fig. 9.2 of Ref. [5].

Figure 2.9 shows two exemplary dispersion relations $\lambda(k)$ for different values of ε. From these it can be seen that if the dispersion relation is formed as on the left, the structure with the wave vector $k = 0$ has the largest growth rate therefore the state is homogeneous in space while on the right the structure with the largest growth rate has a finite wave vector $k \neq 0$ therefore this structure will be periodic in space. If we let $\lambda \in \mathbb{C}$, we can get similar results in time.

2.5 Homoclinic orbits

A homoclinic orbit is a trajectory in the phase space of a dynamical system that converges to a saddle point as time goes to both positive and negative infinity. A saddle point or hyperbolic fixed point is a fixed point without a center manifold, so all eigenvectors either converge or diverge exponentially fast to or go away from the fixed point [7].
For example, the system:

$$\begin{aligned}\dot{x} &= y \\ \dot{y} &= x - x^2\end{aligned} \tag{2.12}$$

has a homoclinic orbit in the half-plane $x \geq 0$. This is illustrated in Fig. 2.10.

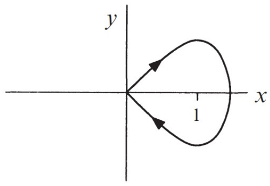

Figure 2.10: An example of a homoclinic orbit of the system (2.12). First the trajectory moves away from the saddle point at (0,0) and then returns. This figure has been adapted from Fig. 6.6.6 of Ref. [7].

A trajectory can then be formed which first leaves the fixed point on the unstable manifold and then changes to the stable manifold and returns to the fixed point. This is called a homoclinic orbit.

2.6 Localized structures

Localized states (LSs) are spatially confined structures that arise in nonlinear systems due to the coexistence of different stable states. LSs often can be understood as homoclinic orbits in the spatial dynamics of the system.
Figure 2.11 illustrates the correspondence between a pattern-element LS and a homoclinic orbit. In panel (a), a pattern-element LS with a plateau of length L asymptotic to the homogeneous steady state is shown. Panel (b) depicts the associated homoclinic orbit in spatial dynamics, where the

trajectory leaves the homogeneous state, turns around the pattern (indicated by the cycle), and returns to the homogeneous state.

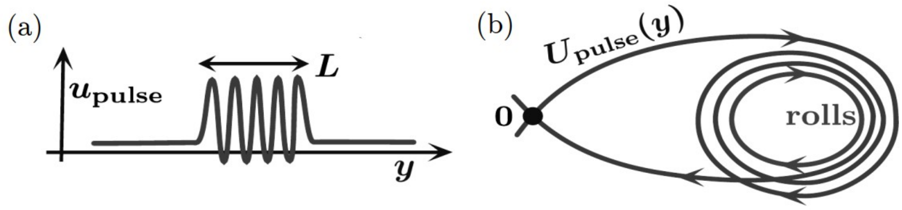

Figure 2.11: Correspondence between a pattern-element LS and homoclinic orbit in the context of spatial dynamics. In (a) a pattern-element type of LS, with a plateau of length L biasymptotic to the homogeneous state is shown. In (b), the associated homoclinic orbit in the spatial dynamics. A trajectory leaves the homogeneous state, turns several times around the pattern (rolls), and returns back to the homogeneous state. This figure has been adapted from Figure 2.1 of Ref. [13].

2.6.1 Spatial eigenvalues and interaction of LSs

Localized structures (LSs) in nonlinear systems often exhibit oscillatory tails, which are regions where the amplitude of the structure decays in an oscillatory manner as it approaches the homogeneous state. Examples of oscillatory tails are Depicted in Fig 2.12. These oscillatory tails arise due to the complex eigenvalues of the linearized system around the homogeneous state, called the spatial Eigenvalues.
The calculation of spatial eigenvalues can be obtained by:

1. **Linearization of the system**: First, the nonlinear system (2.9) is linearized around a homogeneous state. This leads to a linear differential equation of the form:

$$\mathcal{L}\psi = \lambda\psi \tag{2.13}$$

where $\mathcal{L}$ is a linear operator describing the system, and ψ, λ are the corresponding eigenfunctions and eigenvalues.

2. **Characteristic equation**: The eigenvalues λ are determined by solving the characteristic equation derived from the linear differential equation.

This equation has the form:

$$\det(\mathcal{L} - \lambda I) = 0 \tag{2.14}$$

where I is the identity matrix and det denotes the determinant operator.

The spatial eigenvalues can be real or complex. For LSs, the spatial eigenvalues determine the behavior of the oscillating edges of the solution. Complex eigenvalues lead to oscillatory tails, while real eigenvalues lead to monotonically decaying tails. If the spatial eigenvalues consist of a purely imaginary doublet the growth rate is zero, so no oscillatory tails can be formed [14].

Examples of the different types of tails are summatized in Fig. 2.12.

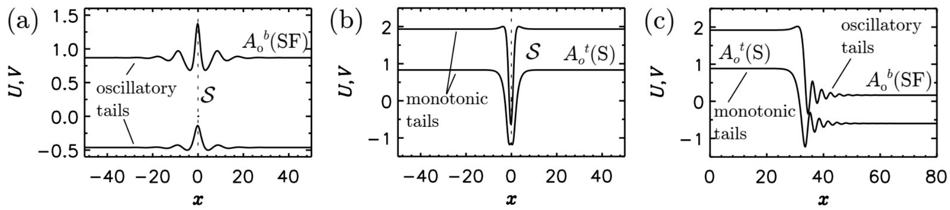

Figure 2.12: Visualization of the tails of different LSs. As we can observe, structure (a) has oscillatory tails, (b) monotonic ones and (c) both. This figure has been adapted from Fig. 2.8 of Ref. [13].

The eigenvalues can be categorized into different groups based on their characteristics. These are depicted in Fig. 2.13.

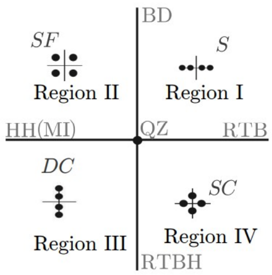

Figure 2.13: Sketch of the possible organization of spatial eigenvalues λ. This figure has been adapted from figure 2.3 of Ref. [13].

This figure shows a sketch of the possible organization of spatial eigenvalues λ, with different regions corresponding to various types of eigenvalue configurations. The most important constellations for this thesis are:

1. **Saddle-Focus (SF)**: This configuration, represented by $(\pm q_0 \pm ik_0)$, corresponds to a system with both real and imaginary eigenvalues. The real part leads to exponential growth or decay, while the imaginary part induces oscillatory behavior. This combination typically results in localized structures with oscillatory tails, which are an essential feature in pattern formation.

2. **Saddle (S)**: The eigenvalues $(\pm q_1, \pm q_2)$ are purely real, indicating exponential growth or decay in multiple directions. This configuration is associated with an unstable saddle point, where the system's solutions exhibit growth along certain directions and decay along others, leading to possible bifurcations or instability.

3. **Double-Center (DC)**: This configuration, with eigenvalues $(\pm ik_1, \pm ik_2)$, involves purely imaginary eigenvalues. It indicates a system with neutral stability and oscillatory behavior in two different directions. This is commonly seen in systems with rotational symmetry, where periodic patterns or structures can emerge.

4. **Saddle-Center (SC)**: Represented by the eigenvalues $(\pm q_0, \pm ik_0)$, this configuration combines both real and imaginary components. The real part leads to exponential growth or decay, while the imaginary part causes oscillations. This combination is crucial for the formation of localized structures with both exponential and oscillatory behavior.

Configurations with codimension greater than zero (Cod > 0), such as Belyakov-Devaney (BD), Hamiltonian-Hopf (HH), and Quadruple Zero (QZ), are not relevant for the focus of this thesis and are therefore not discussed further.

When two LSs are in close proximity, their oscillatory tails can overlap and interact. This interaction determines the stable distances between LSs and the characteristic snaking structure in the bifurcation diagram, as depicted in, e.g. Fig. 3.1.

2.7 Maxwell-point and Lyapunov Functional

The Lyapunov functional is a scalar functional that decreases along the trajectories of the system. Its physical significance, at least in equilibrium thermodynamics, is analogous to that of free energy. In this thesis, the Lyapunov functional is also interpreted as an energy [5]. The Lyapunov functional $F[u(x)]$ is defined as the functional derivative:

$$\frac{\partial u(x)}{\partial t} = -\frac{\delta F[u(x)]}{\delta u(x)} \tag{2.15}$$

and must be limited downwards.
For example Eq.(3.3) with $d_3 = 0$ the Lyapunov functional, reads:

$$F[u] = \int_x \left[-y_0 u - \frac{d_4}{2} \left(\left(\partial_x^2 + \frac{d_2}{2\, d_4} \right) u \right)^2 - \left(\frac{c_1}{2} - \frac{d_2^2}{4\, d_4} \right) u^2 + \frac{1}{4} u^4 \right] \mathrm{d}x. \tag{2.16}$$

The corresponding derivation can be found in chapter A.2.
In the context of homoclinic snaking, the Maxwell point represents the point where the energy of the periodic solution is equal to the energy of the homogeneous state. The low energy gap between periodic and homogeneous state favors the formation of homoclinc orbits and thus snaking in the vicinity of the Maxwell point.

2.8 Numerical path-continuation

Numerical continuation is a method for bifurcation analysis in ordinary and partial differential equations. This technique makes it possible to track stationary states of a system as a function of control parameters and to determine their stability. The main motivation for using numerical continuation is to understand the behavior of a system as a control parameter is varied and to identify critical points, such as bifurcations, where the qualitative behavior of the system changes [15].

2.8.1 Newton method

Newton's method is an iterative method for solving nonlinear equations of the form $f(x) = 0$. It is crucial for numerical continuation. In one dimension, it is based on the Taylor expansion:

$$x_{i+1} = x_i - \frac{f(x_i)}{f'(x_i)}.$$

where x_i represents the approximation of the solution at the i-th iteration, and x_{i+1} is the updated approximation after one iteration. The index i denotes the iteration count, starting from an initial guess x_0. The process is repeated, with the solution being refined at each step, until the method converges to a solution where $f(x) \approx 0$.

For a system of equations $F(x, \lambda) = 0$, the method can be generalized to several dimensions:

$$J(x_i, \lambda)\Delta x_i = -F(x_i, \lambda),$$

where J is the Jacobian matrix:

$$J = \frac{\partial F}{\partial x}$$

and λ is a parameter or set of parameters that influence the system of equations.

2.8.2 General problem for parameter continuation

Suppose we now have a system of n unknowns x that depends on a free parameter λ:

$$\frac{dx}{dt} = F(x, \lambda).$$

For each value of λ, stationary states x (equilibrium, fixed points) can exist, which are defined by $\frac{dx}{dt} = 0$, i.e. $F(x, \lambda) = 0$. And we assume that we have a fixed point for a parameter value $\lambda = \lambda_0$ at $x = x_0$, i.e:

$$F(x_0, \lambda_0) = 0.$$

2.8.3 Steps of the continuation

The aim of numerical path-continuation is to follow the solution (x_0, λ_0) as a function of a parameter λ. The single steps are:

1. **Tangent prediction**: The tangent direction at the solution curve is

determined by differentiating $F(x(\lambda), \lambda) = 0$ w.r.t. λ:

$$\frac{dF}{d\lambda} = \frac{\partial F}{\partial x}\frac{\partial x}{\partial \lambda} + \frac{\partial F}{\partial \lambda} = 0.$$

This leads to a linear system of equations for the tangent vector $\frac{\partial x}{\partial \lambda}$:

$$J\frac{\partial x}{\partial \lambda} = -\frac{\partial F}{\partial \lambda},$$

where J is the Jacobian matrix:

$$J = \frac{\partial F}{\partial x}.$$

2. **Newton correction**: After the tangent prediction, the Newton method is used to refine the approximation:

$$J(x_{i+1}, \lambda_{i+1})\Delta x_{i+1} = -F(x_{i+1}, \lambda_{i+1}).$$

2.8.4 Pseudo arc-length continuation

To overcome problems with pursuing saddle-node bifurcations, the arc length s is introduced as a new control parameter. The system is extended by considering λ as an additional component of the solution vector $x = (x, \lambda)$:

$$\mathcal{E}(x, s) = \begin{bmatrix} F(x, \lambda) \\ p(x, \lambda, s) \end{bmatrix} = 0,$$

where $p(x, \lambda, s)$ is the arc length condition:

$$p(x, \lambda, s) = (x_{j+1} - x_j)\frac{dx}{ds} + (\lambda_{j+1} - \lambda_j)\frac{d\lambda}{ds} - \Delta s = 0.$$

The Jacobian matrix of the extended system is

$$\mathcal{J} = \begin{bmatrix} J & \frac{\partial F}{\partial \lambda} \\ \frac{dx}{ds} & \frac{d\lambda}{ds} \end{bmatrix}.$$

There are several software packages for numerical continuation, in this thesis pde2path is the framework for the continuation of partial differential equations [16].

2.9 Split-step method

For numerical path continuation, a known starting point is assumed. This starting point can, for example, come from a known analytical solution. If such a solution is not available, it can be approximated using numerical methods. One way to achieve this with sufficiently small numerical error is the Fourier-based split-step method. The split-step method is a numerical technique for solving non-linear PDEs. It is often used in optics and quantum mechanics, especially to simulate the propagation of waves in nonlinear media [17].
The method is based on the idea of splitting the PDE into two parts: a linear and a nonlinear part. These parts are then integrated alternately over small time steps. Various methods are used to integrate the two terms. Usually, the linear term is transformed into Fourier space, which allows us to take advantage of the fact that a derivative corresponds to a multiplication in Fourier space, which is more efficient to calculate. The nonlinear terms are calculated separately in real space, since the multiplication corresponds to a convolution in Fourier space.

1. **Decomposition of the PDE**: The PDE is split into a linear part L and a non-linear part N:

$$\frac{\partial u}{\partial t} = L(u) + N(u).$$

2. **Half step for the linear part**: The linear part is integrated over half a time step $\Delta t/2$ in Fourier space:

$$\hat{u}(k, t + \Delta t/2) = \hat{u}(k, t) \exp\left(\frac{\Delta t}{2} L(\hat{k})\right).$$

   Here, $\hat{u}(k, t)$ denotes the Fourier transform of $u(x, t)$, and k represents the wave number. Subsequently, $\hat{u}(k, t + \Delta t/2)$ can be transformed back into real space using the inverse Fourier transform.

3. **Full step for the nonlinear part**: The nonlinear part is integrated over a complete time step Δt in real space:

$$u(x, t + \Delta t) = u(x, t + \Delta t/2) + \Delta t N(u(x, t + \Delta t/2))$$

4. **Second half-step for the linear part**: The linear part is integrated again over half a time step $\Delta t/2$ in Fourier space:

$$\hat{u}(k, t + \Delta t) = \hat{u}(k, t + \Delta t/2) \exp\left(\frac{\Delta t}{2} \hat{L(k)}\right).$$

Finally, the inverse Fourier transform is applied to obtain the final solution in real space.

Chapter 3

Model system

This thesis deals with the impact of high-order effects on the dynamics of localized states in the Swift-Hohenberg equation (SHE). The SHE is a nonlinear partial differential equation (PDE) that is particularly suitable for describing pattern formation processes, such as the formation of fingerprints or the formation of grooves on drying raisins [3, 18]. Another example of a system where the Swift-Hohenberg equation is applicable is the study of hydrodynamic fluctuations at a convective instability. This phenomenon occurs in fluid systems where thermal convection leads to pattern formation. The Swift-Hohenberg equation can describe the onset of convection and the resulting patterns in such systems [1]. Its general form in one spatial dimension reads:

$$\partial_t u = ru - (\partial_x^2 + k_c^2)^2 u + vu^2 - u^3, \tag{3.1}$$

where $u = u(x,t)$ is a scalar real field, r and v are real-valued control parameters and k_c is the critical wavenumber [4]. This equation leads to typical solutions like steady (homogeneous) solutions where $u = \text{const}$, spatiallyperiodic solutions or localized states. A particularly interesting phenomenon that occurs in this equation is homoclinic snaking.

Homoclinic snaking refers to the phenomenon where localized structures in a spatially extended system appear and disappear as a parameter is varied. The term “snaking” comes from the characteristic shape of the bifurcation diagram, where the branches of solutions snake back and forth. This behavior has been observed in various systems governed by the Swift-Hohenberg equation, including fluid dynamics [4] and optical cavities [2].

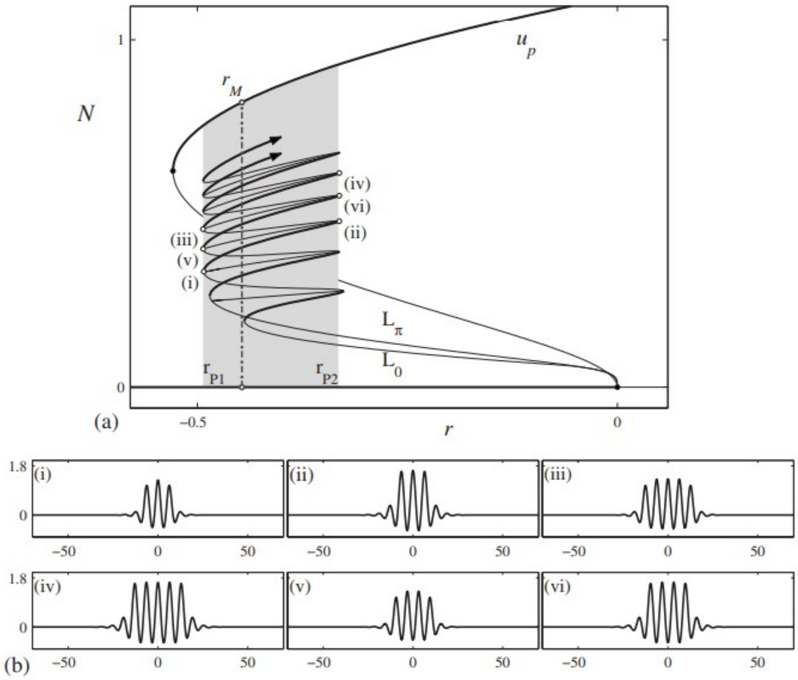

Figure 3.1: (a) Homoclinic snaking in Eq.(3.1) when $v = 2$. Stable (unstable) states are indicated by thick (thin) lines. N is the L^2 norm per unit length. (b) Sample localized profiles $u(r)$. States (i)–(iv) are located at successive saddle-nodes on the L_0 branch; (v)–(vi) lie on L_π branch. The LSs with an odd number of peaks can be seen on the L_0 branch while the LSs with an even number of peaks are located on the L_π branch. This figure has been adapted from Figure 8 of Ref. [6].

In Fig. 3.1 a bifurcation diagram in r of the classical SHE (3.1) is shown as an example. The snaking structures are clearly recognizable and the Maxwell point (vertical dotted line) is in the immediate vicinity, which was to be expected according to chapter 2.7 as no LSs are possible far away from the Maxwell point. The interaction of the oscillating tails of the LSs determines the stable distances between the LSs and thus the characteristic snaking structure in the bifurcation diagram.
For optical systems, one can derive a special form of the SHE. This form results from the study of optical resonators [2]. For certain parameter ranges, the following formulation of the SHE results:

$$\frac{\partial u}{\partial t} = y_0 + c_1\, u - u^3 + d_2 \frac{\partial^2 u}{\partial x^2} + d_4 \frac{\partial^4 u}{\partial x^4} \tag{3.2}$$

where the parameters y_0 and c_1 are deviations of the amplitude of the injected field and the cavity detuning from their critical values at the onset of the modulational instability, respectively. The parameters d_2 and d_4 stem from the second- and fourth-order dispersion relation.
Both forms of the SHE equation are equivalent and can be transformed into each other. To prove this, we perform a transformation from Eq.(3.1) into the Eq.(3.2), see chapter 3.2.
In this thesis, we want to analyze the impact of high-order effects on the dynamics of localized states in optical form of the SHE. To do this, we add a third order term to Eq.(3.2). This results in:

$$\frac{\partial u}{\partial t} = y_0 + c_1\, u - u^3 + d_2 \frac{\partial^2 u}{\partial x^2} + d_3 \frac{\partial^3 u}{\partial x^3} + d_4 \frac{\partial^4 u}{\partial x^4} \tag{3.3}$$

where the parameters y_0, c_1, d_2 and d_4 are the same as in Eq.(3.2) and d_3 controls the third-order dispersion relation. Since the spatial derivatives do not affect homogeneous states, the homogeneous states of Eq. (3.2) and Eq. (3.3), as derived in chapter 3.1, are identical. In chapter 3.1, we show that the analytical description of the homogeneous states of Eq. (3.3) can be derived with relative ease.

3.1 Homogeneous states

The analytical derivation of solutions of nonlinear equations is generally difficult, but the Eq.(3.3) is very simplified for the homogeneous states. A homogeneous state is a state where u is constant in time and has no spatial dependence. This means that $\frac{\partial u}{\partial t} = 0$ and all spatial derivatives of u are also zero. Substituting this into Eq.(3.3), we get:

$$0 = y_0 + c_1\, u - u^3. \tag{3.4}$$

This equation can be rearranged to:

$$u^3 - c_1\, u - y_0 = 0. \tag{3.5}$$

To find the solutions of the cubic equation, we use the general solution formula for cubic equations. The cubic equation has the form

$$u^3 + a\,u^2 + b\,u + c = 0. \tag{3.6}$$

In our case, $a = 0$, $b = -c_1$ and $c = -y_0$. The solutions can be found using the Cardano formula.

1. First Solution:

$$u_0 = -\left(\frac{2 \cdot 3^{1/3} \cdot c_1 + 2^{1/3} \cdot \left(-9 \cdot y_0 + \sqrt{-12 \cdot c_1^3 + 81 \cdot y_0^2}\right)^{2/3}}{6^{2/3} \cdot \left(-9 \cdot y_0 + \sqrt{-12 \cdot c_1^3 + 81 \cdot y_0^2}\right)^{1/3}}\right) \tag{3.7}$$

2. Second Solution:

$$u_1 = \frac{(-2) \cdot (-3)^{2/3} \cdot c_1 + (-6)^{1/3} \cdot \left(-9 \cdot y_0 + \sqrt{-12 \cdot c_1^3 + 81 \cdot y_0^2}\right)^{2/3}}{3 \cdot 2^{2/3} \cdot \left(-9 \cdot y_0 + \sqrt{-12 \cdot c_1^3 + 81 \cdot y_0^2}\right)^{1/3}} \tag{3.8}$$

3. Third Solution:

$$u_2 = (-1)^{1/3} \cdot \frac{2 \cdot 3^{1/3} \cdot c_1 - (-2)^{1/3} \cdot \left(-9 \cdot y_0 + \sqrt{-12 \cdot c_1^3 + 81 \cdot y_0^2}\right)^{2/3}}{6^{2/3} \cdot \left(-9 \cdot y_0 + \sqrt{-12 \cdot c_1^3 + 81 \cdot y_0^2}\right)^{1/3}} \tag{3.9}$$

These solutions give us the homogeneous states as functions of the system parameters.

3.2 Transformation from the classical SHE to optical form SHE

In this chapter we want to derive a transformation from Eq.(3.1) to Eq.(3.2). By multiplying out Eq.(3.1) and rewriting the equation we obtain:

$$\frac{\partial u}{\partial t} = \left(r - k_c^4\right) u + vu^2 - u^3 - 2k_c^2 \frac{\partial^2 u}{\partial x^2} - \frac{\partial^4 u}{\partial x^4} = f(u) + d_2 \frac{\partial^2 u}{\partial x^2} + d_4 \frac{\partial^4 u}{\partial x^4} \tag{3.10}$$

Comparing the last two lines leads to

$$f(u) = \left(r - k_c^4\right) u + vu^2 - u^3 \tag{3.11}$$

$$d_2 = -2k_c^2 \tag{3.12}$$

$$d_4 = -1 \tag{3.13}$$

The optical SHE has the form:

$$\frac{\partial u}{\partial t} = g(u) + d_2 \frac{\partial^2 u}{\partial x^2} + d_3 \frac{\partial^3 u}{\partial x^3} + d_4 \frac{\partial^4 u}{\partial x^4} \tag{3.14}$$

where $g(u) = y_0 + cu - u^3$.
We need a transformation for $f(u) \to g(u)$. We make the ansatz $u \to u + u_0$ and define u_0 in such a way that the prefactor of u^2 in $f(u)$ is unconditionally 0:

$$f(u) = \left(r - k_c^4\right) u + vu^2 - u^3 \tag{3.15}$$

$$f(u + u_0) = \left(r - k_c^4\right)(u + u_0) + v(u + u_0)^2 - (u + u_0)^3 \tag{3.16}$$

$$= \left(r - k_c^4\right) u_0 + vu_0^2 - u_0^3 + \left(r - k_c^4 - 3u_0^2 + 2u_0 v\right) u + (v - 3u_0)u^2 - u^3 \tag{3.17}$$

We see that the prefactor of u^2 is $(v - 3u_0)$, so we demand:

$$0 = v - 3u_0 \tag{3.18}$$

$$u_0 = \frac{v}{3} \tag{3.19}$$

Our transformation is therefore $u \to u + \frac{v}{3}$. Inserting u_0 into $f(u + u_0)$ results in:

$$f\left(u + \frac{v}{3}\right) = y_0 + \left(r - k_c^4 + \frac{v^2}{3}\right) u - u^3 \tag{3.20}$$

where we have used and defined $-3u_0^2 + 2u_0 v = \frac{v^2}{3}$:

$$y_0 = \frac{v}{3}\left(r - k_c^4 + \frac{2v^2}{9}\right) \tag{3.21}$$

Due to a constant offset, the time derivative and the spatial derivatives are not affected by this transformation. Overall, we have:

$$\begin{aligned}
\frac{\partial u}{\partial t} &= \left(r - k_c^4\right) u + vu^2 - u^3 - 2k_c^2 \frac{\partial^2 u}{\partial x^2} - \frac{\partial^4 u}{\partial x^4} && (3.22)\\
&= f(u) + d_2 \frac{\partial^2 u}{\partial x^2} + d_4 \frac{\partial^4 u}{\partial x^4} && (3.23)\\
&= y_0 + \left(r - k_c^4 + \frac{v^2}{3}\right) u - u^3 + d_2 \frac{\partial^2 u}{\partial x^2} + d_4 \frac{\partial^4 u}{\partial x^4} && (3.24)\\
&= g(u) + d_2 \frac{\partial^2 u}{\partial x^2} + d_4 \frac{\partial^4 u}{\partial x^4} && (3.25)
\end{aligned}$$

A similar approach can also be used to find a transformation from Eq.(3.2) to Eq.(3.1).

Chapter 4

Results

4.1 General dynamics without third-order effects

In this chapter, we explore the general dynamics of the optical Swift-Hohenberg Eq.(3.3) without the inclusion of the third-order term, i.e. $d_3 = 0$. This analysis provides a foundational understanding of the system's behavior in its more symmetric form. In particular we will examine the phase space and the various states that emerge under these conditions. Exemplary continuations performed with pde2path [16] are shown in the Figs. 4.1 and 4.2. The L^2 norm of the solutions was used and y_0 was chosen as the primary continuation parameter.

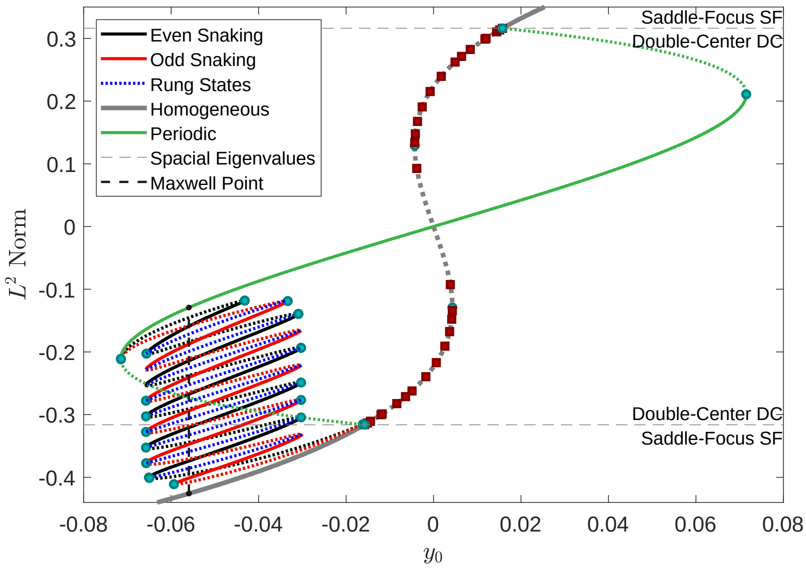

Figure 4.1: The bifurcation diagram of Eq.(3.3) shows the L^2-norm as a function of the injection y_0. Shown are the homogeneous states (gray), periodic states (green) and LS for the parameters $d_2 = d_4 = -1$, $d_3 = 0$, $c_1 = 0.05$. Stable branch sections are marked with solid lines, while the unstable ones are dotted. The gray circles indicate bifurcation points and the red squares indicate Hopf-bifurcation points. The LS form a snaking structure around the Maxwell point at $y_0 \approx -0.0559$ (black dotted line). In the case of snaking, the odd (red) and even (black) branches are shown, as well as the Rung states (blue) that connect the snaking branches. The spatial eigenvalues are plotted according to Fig. 2.13.

In contrast to the classical Swift-Hohenberg equation (3.1) (Fig. 3.1), the homogeneous state in the Fig. 4.1 is not trivial but has an S-shape. In this parameter set, there is no bistable region of the homogeneous branch. The absence of a bistable region in the homogeneous branch means that the system lacks the necessary conditions for the formation of LSs between the homogeneous states. This can significantly simplify the dynamics, leading to fewer transitions between states and a more straightforward phase space. At the bifurcation points of the homogeneous branch where the stability changes, the periodic state also bifurcates from the homogeneous state. This branch has an inverted S-shape and reunites with the homogeneous branch at the other bifurcation point. Although Hopf-bifurcation points (red squares) are drawn on the homogeneous branch, they are not correct because we can define a Lyapunov functional (2.16) for Eq.(3.3) as long $d_3 = 0$. This is because Hopf-bifurcations always lead to periodic orbits, which are impossible due to the Lyapunov functional. The fact that these bifucation points were nevertheless found is due to the way in which pde2path identifies bifurcation points [16]. The bifurcation points are also the values at which the constellation of the spacial eigenvalues changes. In the area where the homogeneous branch is stable, the eigenvalues have a saddle focus (SF) constellation. In the unstable area, they have a double-center (DC) constellation. Further, homoclinic snaking exists in the area in which the spatial eigenvalues of the homogeneous state have an SF constellation. This fits the results of chapter 2.6.1, since complex eigenvalues exist here that lead to the formation of oscillatory tails, which enable the snaking structure. In the area of DC spatial eigenvalues, it can be seen that the homogeneous state is unstable here. This is also to be expected, as the spatial eigenvalues are purely imaginary here, i.e. $\lambda_0 = \pm i k_0$. This means the growth rate for a real k_0 has to be zero. As a consequence, the growth rate must be positive either for $k > k_0$ or for $k < k_0$. Since there are values for k for which the dispersion relation is positive, the homogeneous state is unstable [14].

In Fig. 4.2 the snaking structure from Fig. 4.1 is zoomed in and six exemplary profiles along the snaking are plotted.

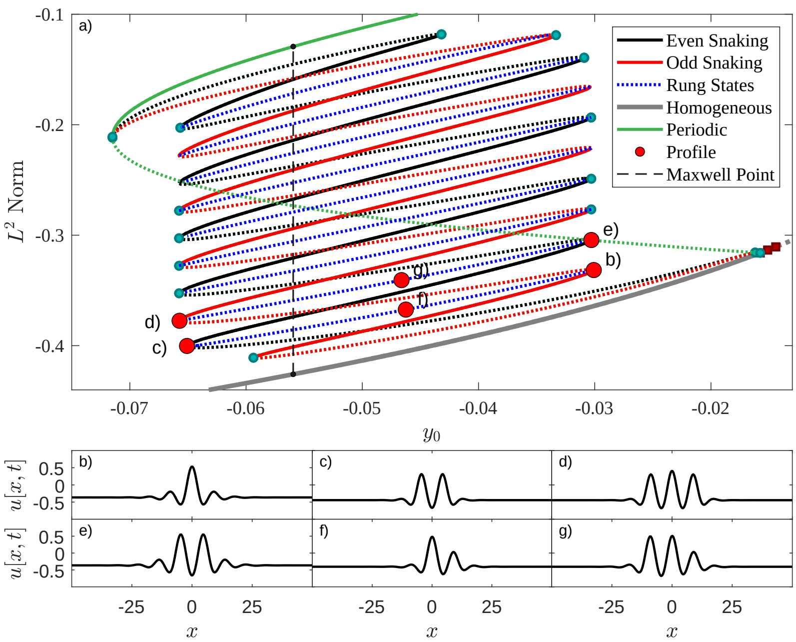

Figure 4.2: Close-up of the snaking region from Fig. 4.1. Sample profiles $u(x,t)$ at the saddle-nodes indicated in a). The points b) and d) lie on the odd snaking branch, while c) and e) lie on the even snaking branch. The points f) and g) are located on the Rung states. The number of soliton peaks increases as the periodic branch is approached.

The snaking structure consists of an odd and an even snaking branch. These both 'snake' around the Maxwell point. The Maxwell point was calculated with Eq.(2.16) and is the point at which the energy of the homogeneous state corresponds to that of the periodic state. Since the homoclinic orbits of the snaking structure can only exist in the vicinity of this point, it is located in the center of this structure. The branches of the Rung states are drawn between the odd and even branches. These each connect a saddle node point of the odd branch with a saddle node point of the even branch. Panels b) - g) show examples of the snaking structure profiles. The profiles of two saddle node points and one rung state have been plotted for both the odd and the even branch. The lowest saddle node points in the odd (b) and even (c) show that the LSs also have the smallest number of peaks here. There is one peak in the odd branch and two in the even branch.

Higher up in the snaking (d), three peaks are increasingly recognizable in the case of the odd branch. This continues until the upper end, where the snaking branches reunite with the periodic branch and the paths of the snaking branches correspond to those of the periodic branches. The example profiles of the Rung states (f) and g) show how a new peak arises or decays at the transition between the odd and even branch, depending on which direction you go. at the transition from point b) to point c), you can see in profile f) how a small peak arises/decays on the right-hand side. Strictly speaking, two possible states are lying on top of each other at the point of the Rung state, one in which the peak arises/decays on the right-hand side and one in which the peak arises/decays on the left-hand side. Since both branches have the same L^2-norm, they lie on top of each other here. Close examination of the profile along the snaking branches reveals that the wavelength of the periodic part of the LS does not exactly match the wavelength of the periodic branch. To investigate this discrepancy further, the peaks in the profiles shown in Fig. 4.2 were identified using the findpeaks function [19]. The average distance between these peaks was then calculated and normalized to the average wavelength λ_c of the periodic branch. The resolution of this method depends on the number of elements into which the domain is divided. To enhance the resolution, the number of elements was increased to 4096.

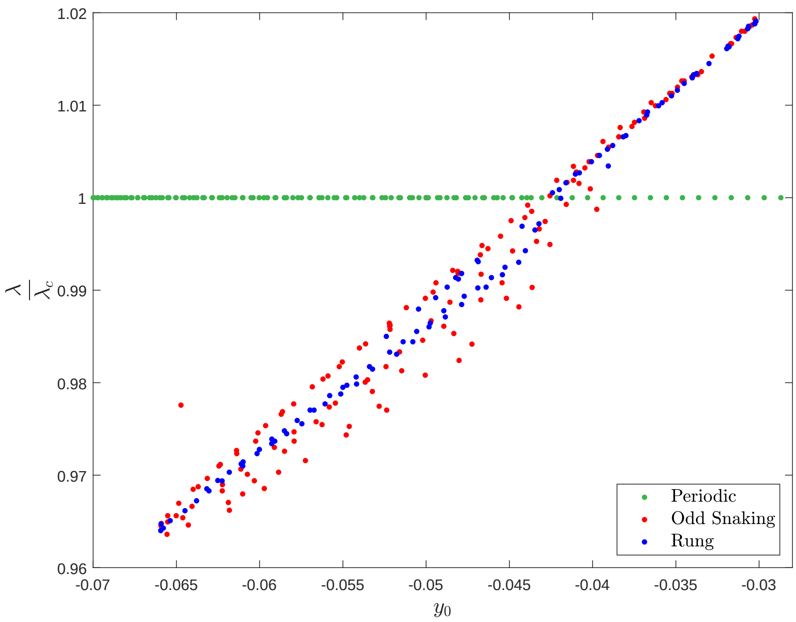

Figure 4.3: The wavelength of the periodic branches (green), the odd snaking branch (red) and the rung states (blue) of Fig. 4.2 is determined and normalized to the mean wavelength of the periodic branch λ_c. This is then plotted against the primary continuation parameter y_0.

In Fig. 4.3, it can be seen that the wavelength of the periodic branch stays constant, while the wavelengths of the odd snaking branch and the rung states vary. This fits in with the findings made in the paper [4]. The wavelength of the periodic part of the LS varies due to the influence of the parameter y_0. At lower y_0 values, where the flat state is energetically favored, the LS is compressed, resulting in a shorter wavelength. Conversely, at higher y_0 values, where the patterned state is favored, the LS expands, leading to a longer wavelength.

4.2 Impact of third order effects

In this chapter, we explore the influence of third-order dispersion on the dynamics of localized states within the framework of Eq.(3.3). The inclusion of a third-order term introduces significant changes to the system's behavior, particularly in terms of wave asymmetry. Due to the resulting asymmetry, the bifurcation points in the homoclinic snaking "break" similar to the pitchfork bifurcation discussed in chapter 2.3.4. Two new saddle node bifurcations are formed. A zoomed-in section of the snaking for different values of d_3 is shown in Fig. 4.4.

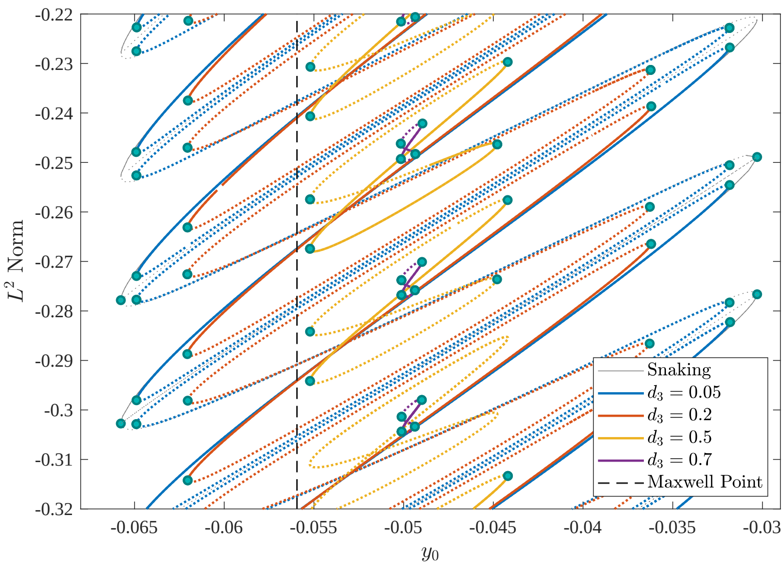

Figure 4.4: Zoom into the snaking branch of Eq. (3.2) as a function as a function of y_0 for different values of d_3. At $y_0 \approx -0.0559$ the black dotted line indicates the Maxwell point. The thin gray line shows the snaking at $d_3 = 0$ as in Fig. 4.2. The parameters were set to $d_2 = d_4 = -1$, $c_1 = 0.05$. Stable branch sections are marked with solid lines, while the unstable ones are dotted. The turquoise circles indicate bifurcation points. The colored lines show the branches at different values of d_3. It can be seen that the saddle node bifurcation points at $d_3 \neq 0$ break up and isolated branches (isolas) are formed. The expansion of the isolas in x- and y-direction shrinks with increasing d_3.

In Fig. 4.4 it can be seen that when the snaking "breaks", isolated branches, so-called isolas, are created that are no longer connected to any other branch. As already mentioned in chapter 4.1, two Rung states lie on top of each other in the bifurcation diagram for $d_3 = 0$. In Fig. 4.4 those move away from each other at $d_3 \neq 0$ and become part of separate isolas. As d_3 increases, the isolas become smaller and smaller. Above a certain d_3 value (here $d_3 > 0.7$), the isolas disappear. The exact value is slightly different for every isola.

4.2.1 Reconnected Isolas

In chapter 4.2 only the parameter y_0 was changed during the continuation. However, we can also choose a different cut through the phase space in which we change both y_0 and another parameter, such as e.g. d_3 during the continuation. In Fig. 4.5, d_3 was chosen to be linearly dependent on y_0 by the relation:

$$d_3 = m\,(y_s - y_0). \tag{4.1}$$

Here, y_s was chosen such that it corresponds to the y_0 value of the Maxwell point, so that the Lyapunov functional (2.16) can still be defined at this point and the Maxwell point still exists.

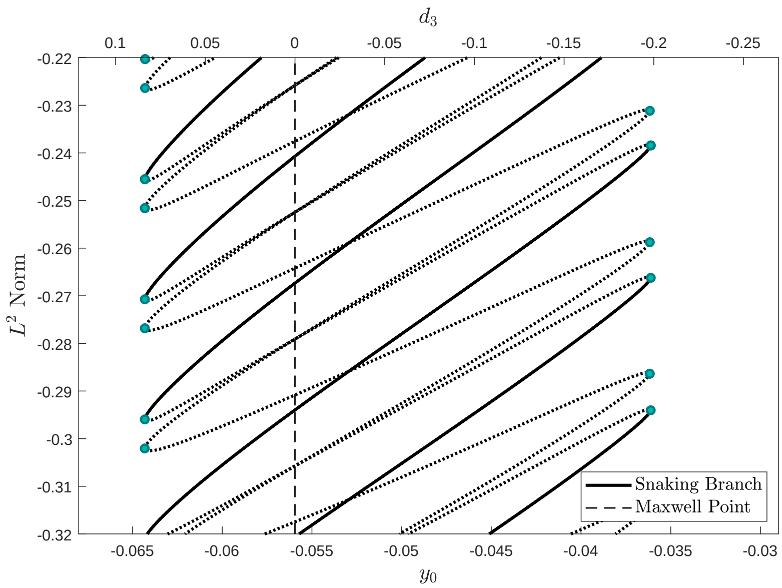

Figure 4.5: Reconnection of the snaking structure when d_3 was made linearly dependent on y_0 by Eq.(4.1) for $m = 10$. The parameter y_s was chosen to be the y_0 value of the Maxwell point. Stable branch sections are marked with solid lines, while the unstable ones are dotted. The turquoise circles indicate bifurcation points. It can be seen that the saddle node bifurcations decay like in Fig. 4.4, but the isolas reconnect at, $y_0 = y_s$ which corresponds to $d_3 = 0$. Other parameters are: $d_2 = d_4 = -1$, $c_1 = 0.05$.

It can be seen that the isolas reconnect at the Maxwell point, at which $d_3 = 0$, thus forming a pair of intertwined branches instead of a stack of isoals.

4.3 Impact of fourth order dispersion relation

In this chapter, we explore the influence of fourth-order dispersion on the dynamics of localized states within the framework of Eq.(3.3). In Fig. 4.6, the snaking structures and periodic branches are plotted for three different values of d_4. It is evident that as d_4 increases, the periodic branch extends to lower y_0 values. Additionally, the Maxwell point shifts towards smaller y_0 values. Specifically, for $d_4 = -1$, the Maxwell point is at $y_0 = -0.055945$; for $d_4 = -0.8$, it is at $y_0 = -0.075546$ and for $d_4 = -0.46$, it is at $y_0 = -0.1759$. The snaking structure follows the Maxwell point. The pinning region, i.e. the area in which the snaking exists, becomes larger. In the example profiles b)-g) of Fig. 4.6 it can be seen, that the wavelength of the periodic solution and the width of the soliton peaks decreases with increasing d_4.

As in the previous chapters, we can further explore the phase space by making d_4 linearly dependent on y_0. This approach allows us to cut diagonally through the phase space. The relationship is given by:

$$d_4 = m\,(y_s - y_0) + d_s, \tag{4.2}$$

where m is the incline and d_s is the start value that d_4 has at the point $y_0 = y_s$. Figure 4.7 shows an exemplary result of a continuation run with $m = 5$, $d_s = -1$ and $y_s = -0.05$. It can be seen that with these parameters, a second snaking structure (SS) is created at lower y_0 values. The pinning region of first snaking (FS) structure is stretched, similar to what is shown in Fig. 4.6.

Both snaking structures lie within the area of the homogeneous branch in which the spatial eigenvalues have an SF configuration. In the exemplary profile plots b)-g) it can be seen that, similar to Fig. 4.6, the wavelength of the periodic solution and the width of the soliton peaks decreases with increasing d_4. However, here the wavelength is continuous like d_4. In order to analyse the wavelength of the different branches in more detail, similar to Fig. 4.3 the wavelengths and peak distances of periodic branches and

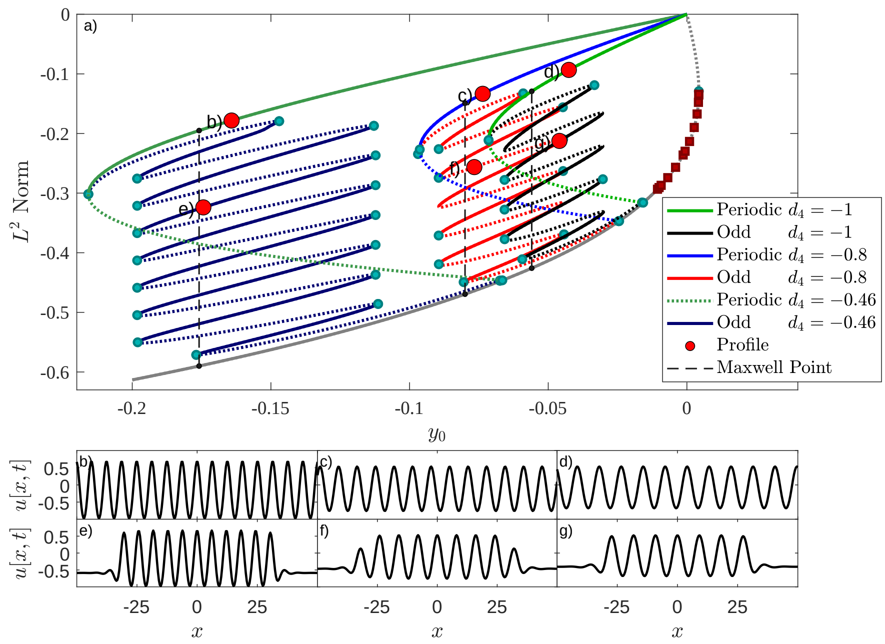

Figure 4.6: Influence of the parameter d_4 on both the periodic and snaking branches of Eq.(3.3). Both branches are shown in a) for different values of d_4, including -1, which corresponds to the value in Fig. 4.2. Stable branch sections are marked with solid lines, while the unstable ones are dotted. The turquoise circles indicate bifurcation points and the red squares indicate Hopf-bifurcation points. For sake of clarity, only the odd snaking branch was plotted in a). The sample profiles b)-g) marked by the red dots in a) show a periodic and an odd profile for each value of d_4. It can be seen that the periodic branch expands towards the sides as d_4 increases. This occurs symmetrically around $y_0 = 0$. The snaking structure also expands and the Maxwell point moves to higher y_0. The sample profiles show that the wavelength of the periodic solution and the width of the soliton peaks decreases with increasing d_4. The other parameters are set to $d_2 = -1$, $d_3 = 0$, $c_1 = 0.05$.

LS from Fig. 4.7 were determined and displayed in Fig. 4.8. Here too, the resolution is determined by the number of elements into which the domain was divided during continuation. A number of 256 elements was selected here. In Fig. 4.8 it can be seen that the wavelength of the periodic branches remains constant, but the wavelength of the snaking structures appears to be dependent on d_4. It has already been shown in the chapter 4.1 in Fig.

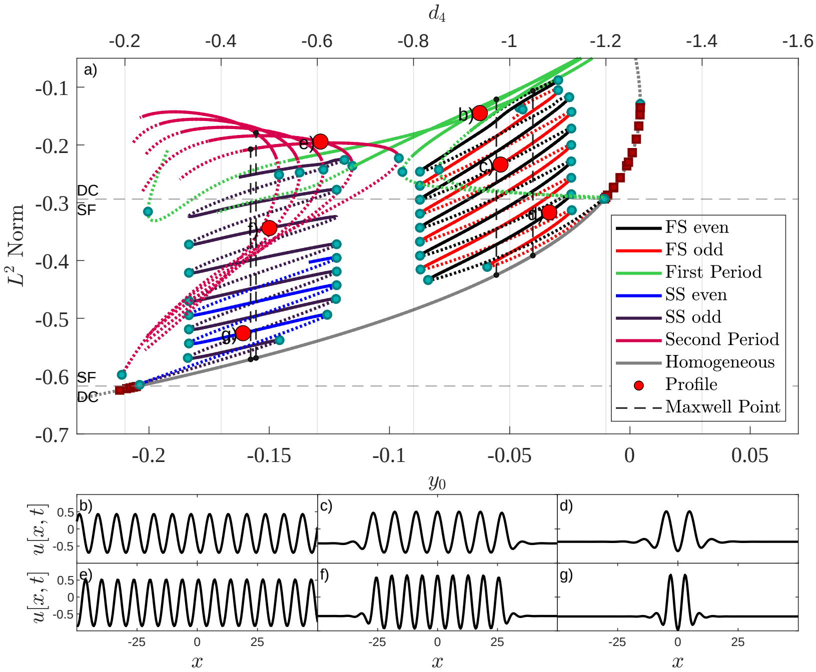

Figure 4.7: Dynamical behavior of Eq.(3.3) when d_4 was made linearly dependent on y_0 by Eq.(4.2) for $m = 5$, $y_s = -0.05$ and $d_s = -1$. Stable branch sections are marked with solid lines, while the unstable ones are dotted. The gray circles indicate bifurcation points and the red squares indicate Hopf-bifurcation points. Two snaking structures and periodic branches are formed in this configuration. The first snaking (FS) consists of homoclinic orbits between one of the first periodic (FP) and the homogeneous branch. The Maxwell points within the FS structure also connect these branches. The second snaking (SS), on the other hand, connects the second period (SP) and the homogeneous branch. In the SS structure are Maxwell points that connect the SP and homogeneous branch. Both snaking structures lie in the area of the homogeneous branch in which the spatial eigenvalues have an SF constellation. In the exemplary profile plots b)-g) it can be seen that, similar to Fig. 4.6, the wavelength of the periodic solution and the width of the soliton peaks decreases with increasing d_4. Other parameters are: $d_2 = -1$, $d_3 = 0$ $c_1 = 0.05$.

4.3 that the wavelength of the LS is not always the same, but differs in Fig. 4.3 by up to 4% from the wavelength of the periodic branch. The deviations from a single periodic branch is much higher. In the vicinity of the snaking branches exist more than just one periodic branch as shown in Fig. 4.7. So

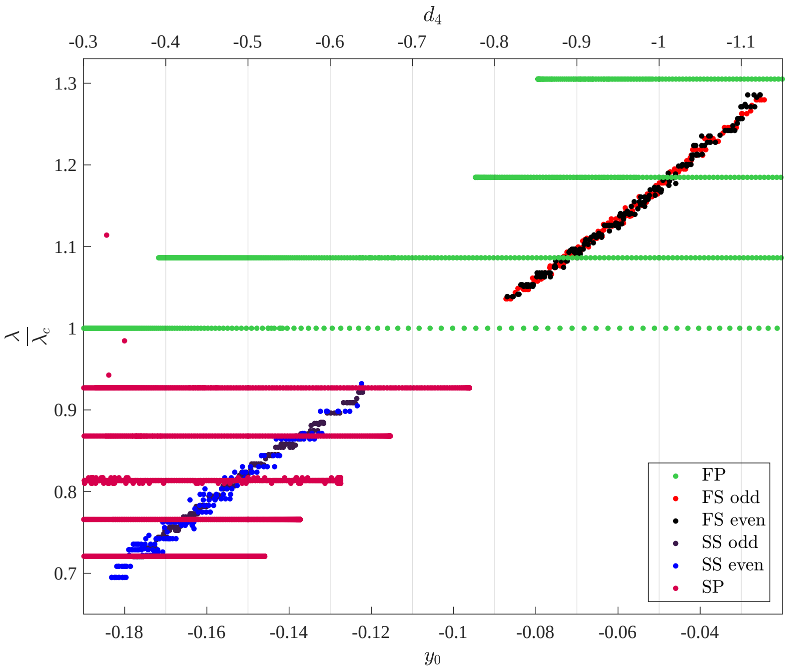

Figure 4.8: The wavelength of the periodic branches (purple/green) and the LSs from Fig. 4.7 is determined and normalized to the wavelength of one of the FP branches λ_c. This is then plotted against the primary continuation parameter y_0 on the lower and d_4 on the upper x-axis.

the homoclinic orbits appear to form around the next periodic branch and not one particular branch. The SS structure consists of homoclinic orbits that form between the second periodic branch (SP) and the homogeneous state. The FS structure consists of homoclinic orbits that form between the first periodic branch (FP) and the homogeneous state. All the different periodic branches have different wavelength as shown in Fig. 4.8. The maxwell points plotted in Fig. 4.7 are the ones from the branch with the greatest and the smallest wavelength of the FP and SP branches. The maxwell points of the periodic branches with intermediate wavelengths lie between the two plotted maxwell points.

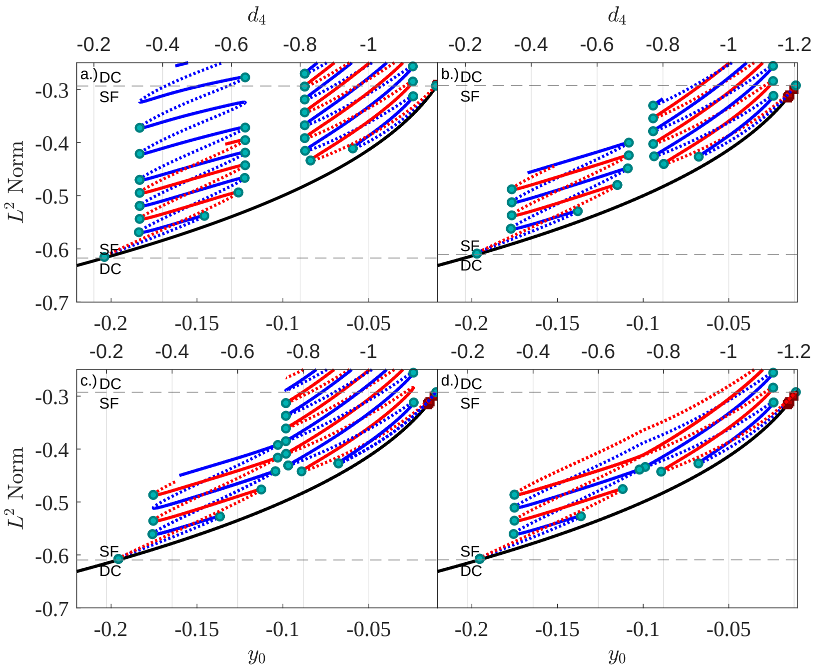

Figure 4.9: Dyanamical behavior of Eq.(3.3) for four different values of m when d_4 was made linearly dependent on y_0 by Eq.(4.2), with $y_s = -0.05$ and $d_s = -1$. With the parameters: $d_2 = -1$, $d_3 = 0$ $c_1 = 0.05$. Stable branch sections are marked with solid lines, while the unstable ones are dotted. The turquoise circles indicate bifurcation points and the red squares indicate Hopf-bifurcation points. In a), $m = 5$ as in Fig. 4.7. In b), $m = 5.2$; in c), $m = 5.24$; and in d), $m = 5.25$. It can be observed that the two snaking structures, FS and SS, move towards each other with increasing m and collide between $m = 5.24$ (c) and $m = 5.25$ (d). During the collision, the even and odd snaking branches of both structures meet their equivalents in the other structure and merge with them. After merging, the branches form overlapping isolas that alternate between even and odd.

If we change the incline m in the Eq.(4.2) we see the behavior shown in Fig. 4.9. Here m was increased. The FS and SS structures move towards each other until they merge at $m \approx 5.25$. The upper windings of the odd and even branches of both structures merge first and form overlapping isolas. The lower windings remain a little longer in a snaking-like structure but are already fused together at the uppermost winding. If m is increased further, isolas are also formed from the lowest turns as shown in Fig. 4.10 for $m = 6.8$.

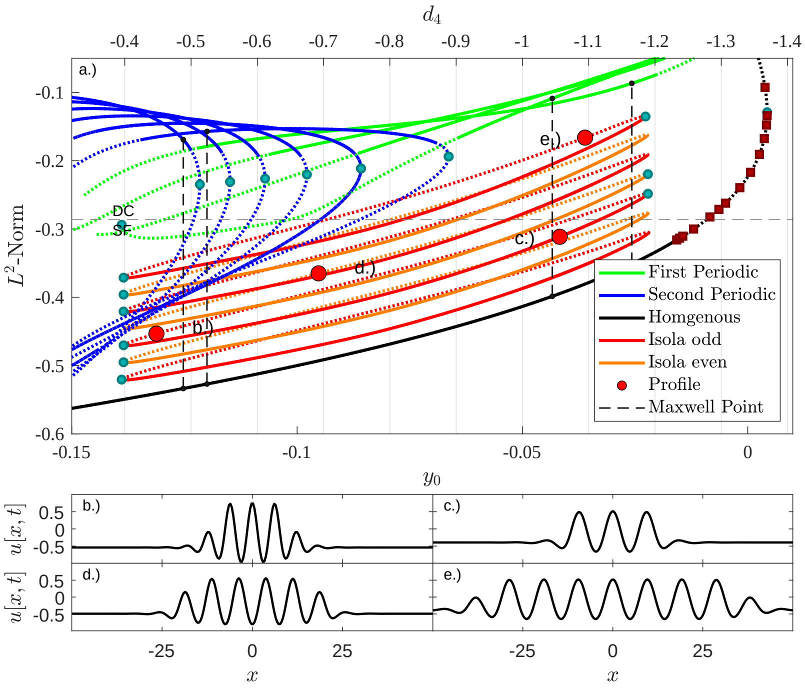

Figure 4.10: Dynamical behavior of Eq.(3.3) for $m = 6.8$ when d_4 was made linearly dependent on y_0 by Eq.(4.2), where $y_s = -0.05$ and $d_s = -1$. Stable branch sections are marked with solid lines, while the unstable ones are dotted. The gray circles indicate bifurcation points and the red squares indicate Hopf-bifurcation points. The two periodic branches are shown with the respective maxwell point. The snaking structures FS and SS have already joined to form isolas at $m = 6.8$ as shown in Fig. 4.9 can be seen. The example profiles b)-e) show the profiles of four selected isolas. Other parameters are: $d_2 = -1$, $d_3 = 0$ $c_1 = 0.05$.

For $m = 6.8$, the collided FS and SS structures result in overlapping isoals that are alternately odd and even. The panels b) and c) with exemplary profiles are on the third isola, d) is on the fourth and e) on the seventh, respectively. It can be seen that, as by snaking, the number of peaks increases with each isola. As in Fig. 4.7 there exist several periodic branches with different wavelength and the Maxwell points plotted in Fig. 4.10 are the ones from the branch with the greatest and the smallest wavelength of the FP and SP branches. The Maxwell points are all located in the area in which the isolas exist, which makes sense, as the LS can only exist in the vicinity of the maxwell points. The example plots also show that, as in

Fig. 4.7, the width of the soliton peaks decreases with increasing d_4. To investigate this further, the wavelength of the periodic branches and LS in Fig. 4.10 was determined and is shown in Fig. 4.11.

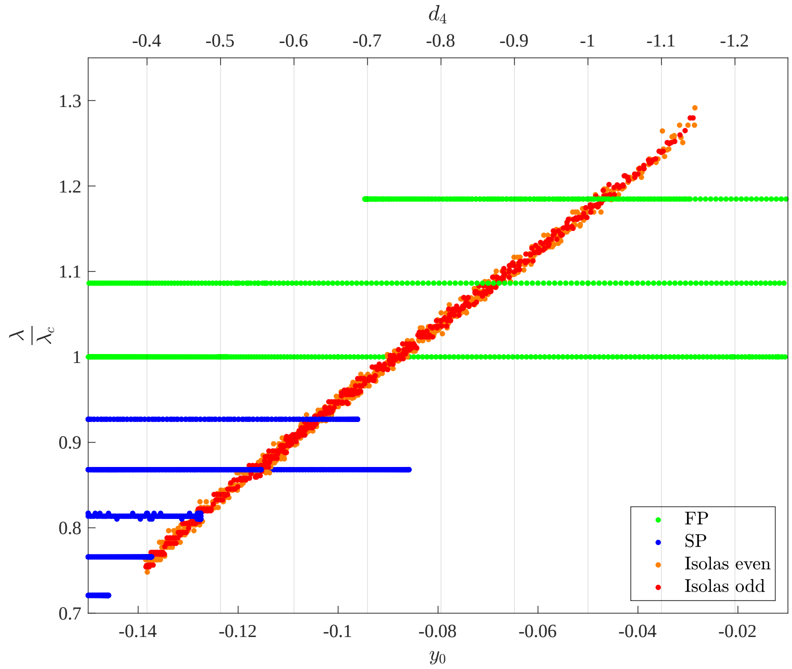

Figure 4.11: The wavelength of the periodic branches (blue/green) and the isolas (red/orange) from Fig. 4.10 is determined and normalized to the wavelength of one of the FP branches λ_c. This is then plotted against the primary continuation parameter y_0 on the lower and d_4 on the upper x-axis.

As in Fig. 4.8 the resolution is determined by the number of elements into which the domain was divided during continuation. A number of 256 elements was selected here. As with $m = 5$, the wavelengths of the periodic states remain constant. As before, the wavelength of the SP is smaller than that of the FP. In contrast to the FS and SS structures in Fig. 4.8 the isolas form a continuous line that intersects the periodic branches.

4.4 Impact of second order contribution

In this chapter, we explore the influence of second-order dispersion on the dynamics of localized states within the framework of Eq.(3.3). As before, we can explore the phase space by making d_2 linearly dependent on y_0. This approach allows us to cut diagonally through the phase space. The corresponding relationship is given by:

$$d_2 = m\,(y_s - y_0) + d_s, \tag{4.3}$$

where m is the incline and d_s is the start value that d_4 has at the point $y_0 = y_s$. Figure 4.12 shows an exemplary result of a continuation for $m = 0$ and $m = 9$.

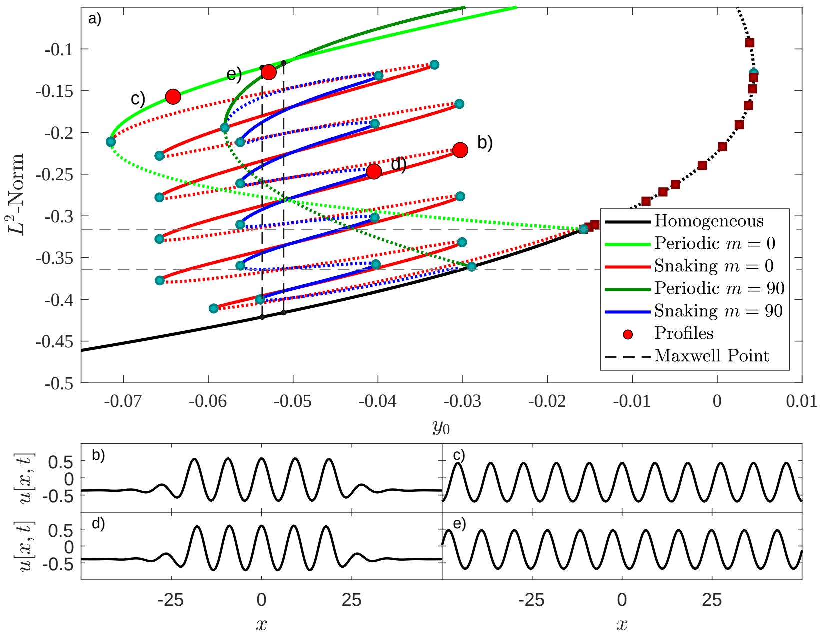

Figure 4.12: Bifurcation diagram of Eq.(3.3) for $m = 0$ and $m = 9$ when d_2 was made linearly dependent on y_0 by Eq.(4.3) and $d_s = -1$. Stable branch sections are marked with solid lines, while the unstable ones are dotted. The gray circles indicate bifurcation points and the red squares indicate Hopf-bifurcation points. The value of y_s was selected as $y_s = -0.05$. It can be seen that the expansion of the periodic branch in the y_0 direction decreases with increasing m. As the snaking structure can only exist in the area of the periodic branch, it is also compressed. The example profiles b)-e) show that the profiles do not change significantly. Other parameters are: $d_3 = 0$, $d_4 = -1$ $c_1 = 0.05$.

In Fig. 4.12, it can be seen that for higher values of m, the snaking is compressed, and the pinning region becomes smaller both to the right and left of $y_s = -0.05$. Additionally, the periodic branch shifts towards higher y_0 values (to the right). The spatial eigenvalues shift, such that the snaking always lies within the range of an SF constellation. In the example profiles b)-e), it can be observed that, unlike in Figure 4.7, the wavelengths of the solutions do not change significantly. Figure 4.13 provides a zoomed-out view of Fig. 4.12, but here $m = 0$ and $m = 2$ are shown.

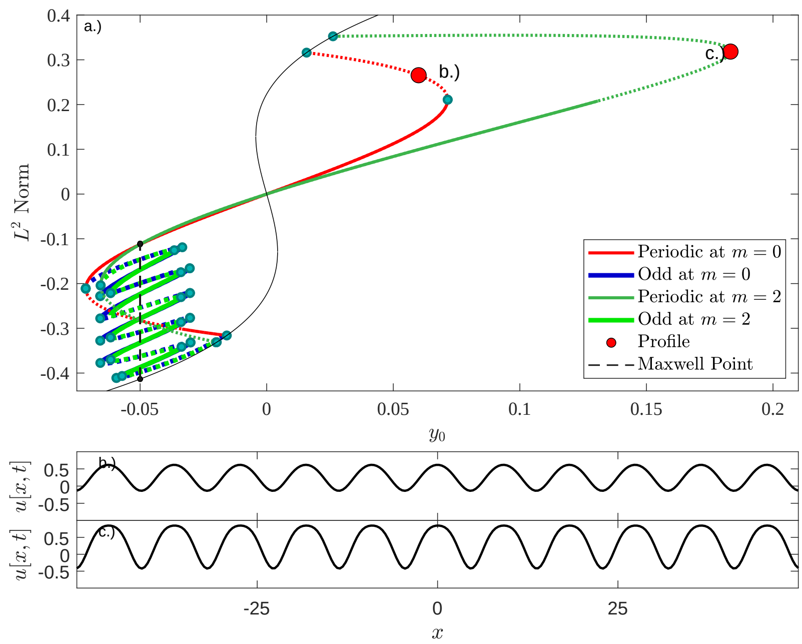

Figure 4.13: Bifurcation diagram of Eq.(3.3) for $m = 0$ and $m = 2$ when d_2 was made linearly dependent on y_0 by Eq.(4.3) with $d_s = -1$. With the parameters: $d_3 = 0$, $d_4 = -1$ $c_1 = 0.05$. Stable branch sections are marked with solid lines, while the unstable ones are dotted. The turquoise circles indicate bifurcation points . The value of y_s was selected as $y_s = -0.05$. Other parameters are: $d_3 = 0$, $d_4 = -1$ $c_1 = 0.05$.

In Fig. 4.13, it can be seen that the periodic branches on the side $y_0 <$ 0 (right) extend in contrast to those at $y_0 > 0$. Also, the extension or compression is not symmetrical, as the extension on the $y_0 > 0$ side is greater than the compression at $y_0 < 0$. This is partly due to the asymmetric choice of $y_s = -0.05$. In Fig. 4.14, the zoomed-out image is shown with $m = 9$.

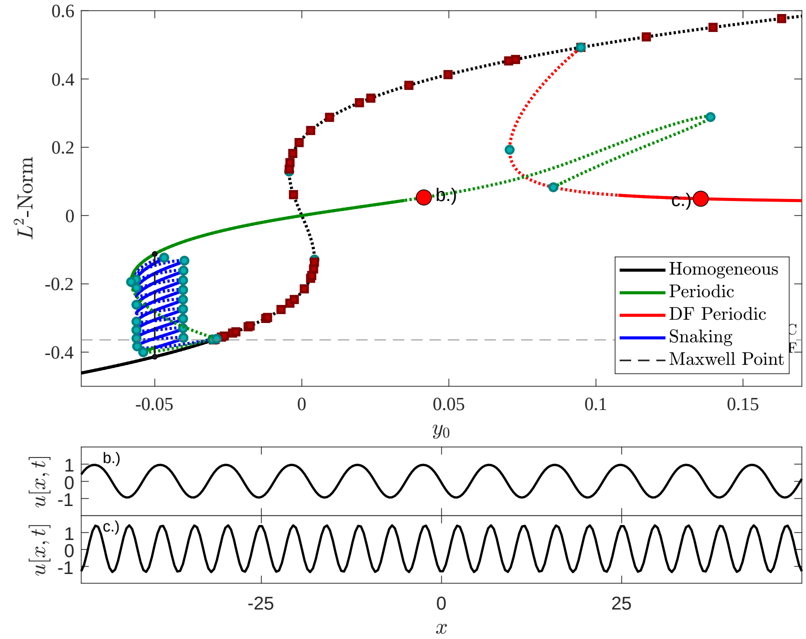

Figure 4.14: Bifurcation diagram of Eq.(3.3) for $m = 9$ when d_2 was made linearly dependent on y_0 by Eq.(4.3) with $d_s = -1$. Stable branch sections are marked with solid lines, while the unstable ones are dotted. The turquoise circles indicate bifurcation points and the red squares indicate Hopf-bifurcation points. The value of y_s was selected as $y_s = -0.05$. Here it can be seen that the periodic branch, after the breaking of the transcritical bifurcation from Fig. 4.15, connects to another branch. The example plots b) and c) show that the wavelength of the new branch corresponds to about half the wavelength of the periodic branch. Other parameters are: $d_3 = 0$, $d_4 = -1$ $c_1 = 0.05$.

In Fig. 4.14, it can be seen that the periodic branch no longer directly merges with the homogeneous state, but forms a new branch that is then connected to both, the periodic and homogeneous branches. In the example panels b) and c), it can be seen that this new branch (c) is also periodic, but has about half the wavelength of the periodic branch (b). This behavior indicates a transcritical bifurcation that lies somewhere between $m = 2$ and $m = 9$. At these values of m, it is either already or not yet 'broken'.

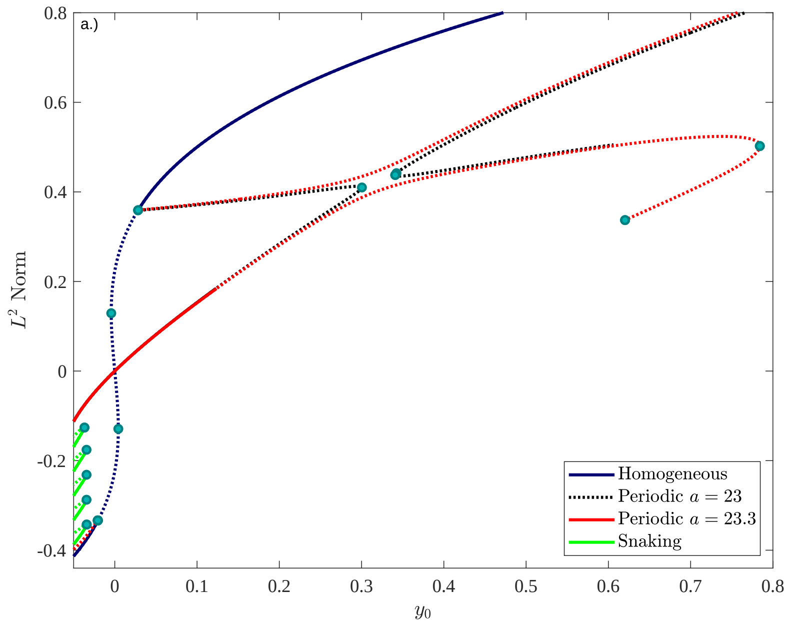

Figure 4.15: Bifurcation diagram of Eq.(3.3) for $m = 2.3$ and $m = 2.33$, when d_2 was made linearly dependent on y_0 by Eq.(4.3) for $d_s = -1$. Stable branch sections are marked with solid lines, while the unstable ones are dotted. The turquoise circles indicate bifurcation points. The value of y_s was selected as $y_s = -0.05$. It can be seen that there is a transcritical bifurcation between the values for m that abruptly changes the behavior of the system here. The periodic branch and another branch connect for a certain value of m, but this bifurcation breaks for all other values. Other parameters are: $d_3 = 0$, $d_4 = -1$ $c_1 = 0.05$.

In Fig. 4.15, the scenario with values for m closer to the transcritical bifurcation is shown. The branches that collide at the bifurcation are also depicted here.

So far, we have considered $m \geq 0$. Now, we want to examine what happens for $m \leq 0$. In Fig. 4.16, an exemplary continuation for $m = -2.35$ is shown.

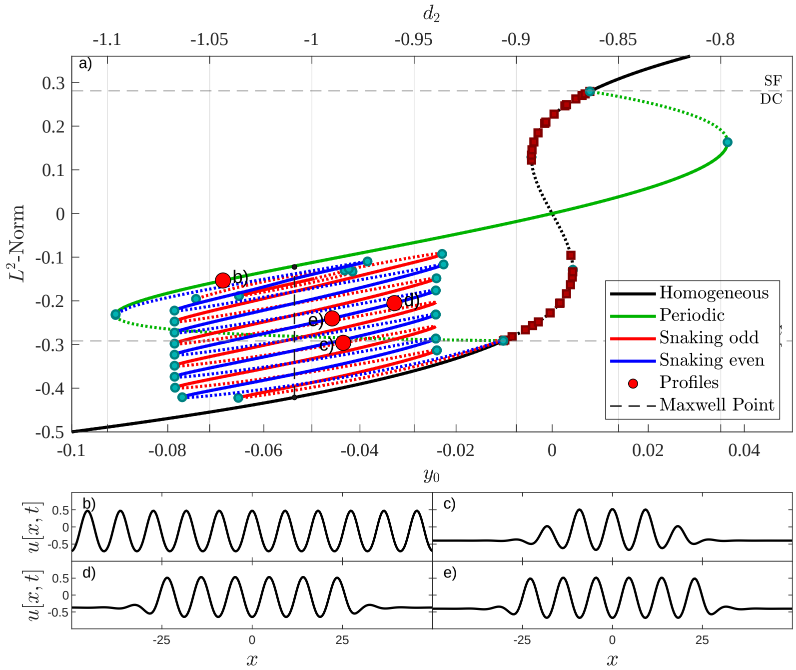

Figure 4.16: Bifurcation diagram of Eq.(3.3) for $m = -2.35$, when d_2 was made linearly dependent on y_0 by Eq.(4.3) for $d_s = -1$. Stable branch sections are marked with solid lines, while the unstable ones are dotted. The turquoise circles indicate bifurcation points and the red squares indicate Hopf-bifurcation points. The value of y_s was selected as $y_s = -0.05$. For negative values of m, it can be seen that the periodic branch and also the snaking structure are now stretched in the y_0 direction. Here too, a transcritical bifurcation occurs symmetrically to the positive values of m, as in Fig. 4.15, of the periodic branch occurs. However, not at $m = -2.35$ this can be explained by the asymmetrically chosen parameter y_s. If $y_s = 0$, the transcritical bifurcation would probably be between $m = 2.3$ and $m = 23.3$ as for positiv m. Other parameters are: $d_3 = 0$, $d_4 = -1$ $c_1 = 0.05$.

For $m = -2.35$, similar to the positive values of m, the periodic branch extends to one side and contracts to the other. However, this occurs in the opposite directions compared to positive m. Additionally, the snaking is now also affected by the stretching, extending along with the periodic branch. In the example panels b)-e), no significant wavelength change is observed, as seen in Fig. 4.7.

To investigate whether a transcritical bifurcation occurs for negative values of m and how the periodic branch detaches from the homogeneous state and how the snaking reacts, $m = -4$ was chosen in Fig. 4.17.

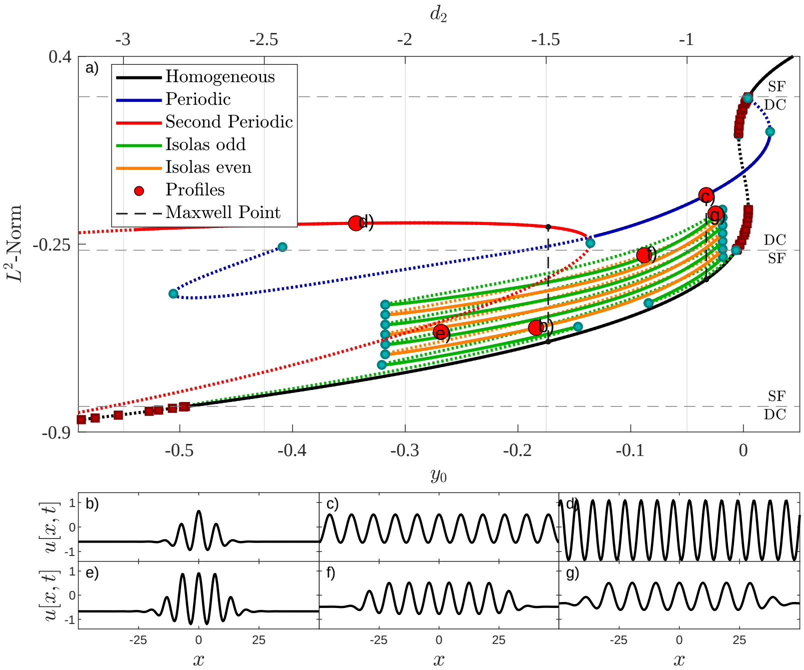

Figure 4.17: Bifurcation diagram of Eq.(3.3) for $m = -4$ when d_2 was made linearly dependent on y_0 by Eq.(4.3), where $d_s = -1$. Stable branch sections are marked with solid lines, while the unstable ones are dotted. The gray circles indicate bifurcation points and the red squares indicate Hopf-bifurcation points. The value of y_s was selected as $y_s = -0.05$. It can be seen that for such low values of m the periodic branch is detached from the homogeneous branch, which indicates a transcritical bifurcation. The snaking structure transitions into overlapping isolas with even and odd isolas alternating. The lowest sections of the branches still exhibit a snaking-like pattern. Other parameters are: $d_3 = 0$, $d_4 = -1$ $c_1 = 0.05$.

In Fig. 4.17, it can be seen that the periodic branch has detached from the homogeneous branch. This suggests that a transcritical bifurcation occurs similarly to the positive values of m. For positive values of m, this bifurcation occurred between $m = 2.3$ and $m = 2.33$. The fact that it has not yet occurred for negative values at $m = -2.35$, as seen in Fig. 4.16, can likely be explained by the asymmetrical choice of y_s. Since this value is not zero, the transcritical bifurcation is likely shifted. The snaking no longer forms a typical snaking structure but overlapping isolas as in Fig. 4.10. Even and odd isolas alternate here too. In 4.17 the lowest sections of the branches still form a snaking-like structure. This looks very similar to the effects that the variation of d_4 had in chapter 4.3, so you could try to find similar effects here as well, such as a second snaking.

Chapter 5

Conclusion and Outlook

In this thesis the impact of high-order effects on the dynamics of localized states in the Swift-Hohenberg Equation (SHE) was investigated. The inclusion of third-order effects (d_3) was found to break homoclinic snaking structures, resulting in the formation of isolated branches (isolas). These isolas were observed to shrink and eventually disappear as d_3 increased. By making d_3 linearly dependent on the control parameter y_0, it was shown that the isolas could reconnect at the point $d_3 = 0$, forming intertwined branches. Fourth-order effects (d_4) significantly influenced the periodic branches and the snaking structures. An increase in d_4 caused a shift in the Maxwell point and an expansion of the pinning region. The exploration of the phase space with d_4 linearly dependent on y_0 revealed the formation of multiple snaking structures and their eventual merging into overlapping isolas.
Second-order contribution (d_2) was found to affect both branches and snaking structures differently. Variations in d_2 revealed the occurrence of transcritical bifurcations, leading to the detachment and reconnection of branches. By making d_2 linearly dependent on the control parameter y_0, the phase space was explored in greater detail. For positive values of m, representing the slope of the linear function, the periodic branch and the snaking structure were compressed in the y_0 direction. This compression reduced the pinning region around the Maxwell point. As m increased, the periodic branch shifted towards higher y_0 values, and the snaking structure became more confined. Transcritical bifurcations were identified for specific values of m, resulting in the detachment and reconnection of branches, which significantly altered the structure of the phase space.

For negative values of m, the periodic branch and snaking structure were stretched in the y_0 direction. This stretching expanded the pinning region, contrary to the behavior observed for positive m. For larger negative values of m, such as $m = -4$, the periodic branch detached from the homogeneous branch, indicating a transcritical bifurcation. This detachment led to the formation of overlapping isolas, with even and odd isolas alternating. The snaking structure transitioned into these isolas.
The study of high-order effects in the Swift-Hohenberg Equation provided several directions for future research. One potential application of these results lies in the injected Kerr-Gires-Tournois Interferometer (KGTI) time delayed system as an order parameter equation, which can be derived near the onset of optical bistability in the anomalous dispersion regime. Further investigations could explore whether negative values of m for d_2 lead to the formation of multiple snaking structures, similar to those observed for d_4, as suggested by the emergence of overlapping isolas.

Appendix A

Further calculations

A.1 Calculation of spatial eigenvalues

The calculation of the spatial eigenvalues was carried out according to the thesis [13].

Assume that u is a complex function such that $u = u_r + iu_i$, where u_r is the real part and u_i is the imaginary part of u.

The original equation is:

$$\frac{\partial u}{\partial t} = y_0 + c_1 \cdot u - u^3 + d_2 \frac{\partial^2 u}{\partial x^2} + d_3 \frac{\partial^3 u}{\partial x^3} + d_4 \frac{\partial^4 u}{\partial x^4} \tag{A.1}$$

Divided into real and imaginary parts we get

$$u = u_r + iu_i. \tag{A.2}$$

The third power of u is then

$$u^3 = (u_r + iu_i)^3. \tag{A.3}$$

Let's expand u^3 using the binomial formulas and the fact that $i^2 = -1$ and $i^3 = -i$:

$$\begin{aligned} u^3 &= (u_r + iu_i)^3 \\ &= u_r^3 + 3iu_r^2 u_i - 3u_r u_i^2 - iu_i^3 \\ &= (u_r^3 - 3u_r u_i^2) + i(3u_r^2 u_i - u_i^3). \end{aligned} \tag{A.4}$$

If we split the original equation into real and imaginary parts, we get
For the real part:

$$\frac{\partial u_r}{\partial t} = y_0 + c_1 u_r - (u_r^3 - 3u_r u_i^2) + d_2 \frac{\partial^2 u_r}{\partial x^2} + d_3 \frac{\partial^3 u_r}{\partial x^3} + d_4 \frac{\partial^4 u_r}{\partial x^4}. \tag{A.5}$$

For the imaginary part:

$$\frac{\partial u_i}{\partial t} = c_1 u_i - (3u_r^2 u_i - u_i^3) + d_2 \frac{\partial^2 u_i}{\partial x^2} + d_3 \frac{\partial^3 u_i}{\partial x^3} + d_4 \frac{\partial^4 u_i}{\partial x^4}. \tag{A.6}$$

We now set the time derivative equal to zero ($\frac{\partial u_r}{\partial t} = 0$ and $\frac{\partial u_i}{\partial t} = 0$) in order to analyse the equilibrium system:
For the real part:

$$0 = y_0 + c_1 u_r - (u_r^3 - 3u_r u_i^2) + d_2 \frac{\partial^2 u_r}{\partial x^2} + d_3 \frac{\partial^3 u_r}{\partial x^3} + d_4 \frac{\partial^4 u_r}{\partial x^4}. \tag{A.7}$$

For the imaginary part:

$$0 = c_1 u_i - (3u_r^2 u_i - u_i^3) + d_2 \frac{\partial^2 u_i}{\partial x^2} + d_3 \frac{\partial^3 u_i}{\partial x^3} + d_4 \frac{\partial^4 u_i}{\partial x^4}. \tag{A.8}$$

Now let's define the new variables:

$$y_1(x) = u_r(x) \tag{A.9}$$

$$y_2(x) = u_i(x) \tag{A.10}$$

$$y_3(x) = \frac{\partial u_r}{\partial x} \tag{A.11}$$

$$y_4(x) = \frac{\partial u_i}{\partial x} \tag{A.12}$$

$$y_5(x) = \frac{\partial^2 u_r}{\partial^2 x} = \frac{\partial y_3}{\partial x} \tag{A.13}$$

$$y_6(x) = \frac{\partial^2 u_i}{\partial^2 x} = \frac{\partial y_4}{\partial x} \tag{A.14}$$

$$y_5(x) = \frac{\partial^3 u_r}{\partial^3 x} = \frac{\partial y_5}{\partial x} \tag{A.15}$$

$$y_8(x) = \frac{\partial^3 u_i}{\partial^3 x} = \frac{\partial y_6}{\partial x} \tag{A.16}$$

The system is reformulated as follows:

$$\frac{\partial y_1}{\partial x} = y_3 \tag{A.17}$$
$$\frac{\partial y_2}{\partial x} = y_4 \tag{A.18}$$
$$\frac{\partial y_3}{\partial x} = y_5 \tag{A.19}$$
$$\frac{\partial y_4}{\partial x} = y_6 \tag{A.20}$$
$$\frac{\partial y_5}{\partial x} = y_7 \tag{A.21}$$
$$\frac{\partial y_6}{\partial x} = y_8 \tag{A.22}$$
$$\frac{\partial y_7}{\partial x} = (-y_0 - c_1 y_1 + (y_1^3 - 3y_1 y_2^2) - d_2 y_5 - d_3 y_7)\frac{1}{d_4} \tag{A.23}$$
$$\frac{\partial y_8}{\partial x} = (-c_1 y_2 + (3y_1^2 y_2 - y_2^3) - d_2 y_6 - d_3 y_8)\frac{1}{d_4}. \tag{A.24}$$
$$\tag{A.25}$$

We summarize the attenuation terms in the parameter ν for a uniform representation of the spatial diffusion. This leads to the Matrix:

$$\begin{bmatrix} 0 & 0 & 1 & 0 & 0 & 0 & 0 & 0 \\ 0 & 0 & 0 & 1 & 0 & 0 & 0 & 0 \\ 0 & 0 & 0 & 0 & 1 & 0 & 0 & 0 \\ 0 & 0 & 0 & 0 & 0 & 1 & 0 & 0 \\ 0 & 0 & 0 & 0 & 0 & 0 & 1 & 0 \\ 0 & 0 & 0 & 0 & 0 & 0 & 0 & 1 \\ \frac{-c_1+3y_1^2-3y_2^2}{d_4} & \frac{-6y_1y_2}{d_4} & 0 & 0 & -\frac{d_2}{2} & 0 & \frac{-d_3}{d_4} & 0 \\ \frac{6y_1y_2}{d_4} & \frac{-c_1+3y_1^2-3y_2^2}{d_4} & 0 & 0 & 0 & -\frac{d_2}{2} & 0 & \frac{-d_3}{d_4} \end{bmatrix}$$

The eigenvalues of the matrix were calculated with Mathematica [20]. However, the expressions are too long to be written here. The structure of the eigenvalues shows that only four possible constellations are possible. These are shown in Fig. 2.13. Here the calculation was done in general for complex u since we can define a Lyapunov functionally in the SHE we know that the imaginary part of u is 0.

A.2 Derivation of the Lyapunov functional

The rhs of Equation (3.2) can be written as the functional derivative:

$$\frac{\partial u(x)}{\partial t} = -\frac{\delta F[u(x)]}{\delta u(x)}. \tag{A.26}$$

In Mathematics $F[u(x)]$ is referred to as the Lyapunov functional.
For Equation (3.2) the Lyapunov functional results in:

$$F[u] = \int_x \left[-y_0 u - \frac{d_4}{2}\left(\left(\partial_x^2 + \frac{d_2}{2\,d_4}\right)u\right)^2 - \left(\frac{c_1}{2} - \frac{d_2^2}{4\,d_4}\right)u^2 + \frac{1}{4}u^4 \right] \mathrm{d}x. \tag{A.27}$$

We see that this functional is lower bounded since the first and third term in the integral can become negative, but the term $\frac{1}{2}u^4$ cannot become negative and for large values of u this non-negative term will be the larger one. The second term can also not be negative as long as $d_4 \leq 0$.
If we multiply out everything we get:

$$F[u] = \int_x \left[-y_0 u - \frac{d_4}{2}(\partial_x^2 u)^2 - \frac{d_2}{2} u \partial_x^2 u - \frac{c_1}{2}u^2 + \frac{1}{4}u^4 \right] dx. \tag{A.28}$$

The Derivative of a functional is defined as:

$$\int_D \frac{\delta F[y]}{\delta y(x)} \phi(x) \mathrm{d}x := \left. \frac{d}{d\varepsilon} F[y + \varepsilon\phi] \right|_{\varepsilon=0}. \tag{A.29}$$

We use (A.29) to calculate the functional derivative of (A.28):

$$\begin{aligned} &\int_x \frac{\delta F[u]}{\delta u(x)} \mu(x)\,\mathrm{d}x = \\ &\frac{d}{d\epsilon}\left(\int_x \left[-y_0[u+\epsilon\mu] - \frac{d_4}{2}(\partial_x^2[u+\epsilon\mu])^2 - \frac{d_2}{2}[u+\epsilon\mu]\partial_x^2[u+\epsilon\mu] \right.\right. \\ &\left.\left. -\frac{c_1}{2}[u+\epsilon\mu]^2 + \frac{1}{4}[u+\epsilon\mu]^4 \right] \right) |_{\epsilon=0}\,\mathrm{d}x. \end{aligned} \tag{A.30}$$

Because ϵ is small we can make a Taylor expansion of $[u + \epsilon\mu]$:

$$T([u+\epsilon\mu]^p) = u^p + p\mu\epsilon u^{p-1} + h.o.t. \tag{A.31}$$

When we put Equation (A.31) into Equation (A.30) we get:

$$= \frac{d}{d\epsilon}\left(\int_x \left[-y_0[u+\epsilon\mu] - \frac{d_4}{2}(\partial_x^2[u+\epsilon\mu])^2 - \frac{d_2}{2}[u+\epsilon\mu]\partial_x^2[u+\epsilon\mu] \right.\right. \tag{A.32}$$
$$\left.\left. -\frac{c_1}{2}[u^2+2\mu\epsilon u] + \frac{1}{4}[u^4+4\mu\epsilon u^3]\right]\right)|_{\epsilon=0}\,\mathrm{d}x.$$

We can drag the derivative into the integral and multiply out the parenthesis. This gives us:

$$\begin{aligned}= \int_x \frac{\partial}{\partial\epsilon}\Big[&-y_0 u - y_0\epsilon\mu - \frac{d_4}{2}\left((\partial_x^2 u)^2 + 2\epsilon\partial_x^2 u\partial_x^2\mu + \epsilon^2(\partial_x^2\mu)^2\right) \\ &- \frac{d_2}{2}\left(u\partial_x^2 u + \epsilon\mu\partial_x^2 u + \epsilon u\partial_x^2\mu + \epsilon^2\mu\partial_x^2\mu\right) \\ &-\frac{c_1}{2}u^2 - \frac{c_1}{2}2\mu\epsilon u + \frac{1}{4}u^4 + \frac{1}{4}4\mu\epsilon u^3\Big)\Big]\Big|_{\epsilon=0}\,\mathrm{d}x.\end{aligned} \tag{A.33}$$

After the derivation to epsilon, remains:

$$\begin{aligned}= \int_x \Big[&-y_0\mu - \frac{d_4}{2}\left(2\partial_x^2 u\partial_x^2\mu + 2\epsilon(\partial_x^2\mu)^2\right) - \frac{d_2}{2}\left(\mu\partial_x^2 u + u\partial_x^2\mu + 2\epsilon\mu\partial_x^2\mu\right) \\ &-\frac{c_1}{2}2\mu u + \mu u^3\Big)\Big]\Big|_{\epsilon=0}\,\mathrm{d}x.\end{aligned} \tag{A.34}$$

If we set $\epsilon = 0$:

$$= \int_x \left[-y_0\mu + \frac{d_4}{2}\left(2\partial_x^2 u\partial_x^2\mu\right) + \frac{d_2}{2}\left(\mu\partial_x^2 u + u\partial_x^2\mu\right) + \frac{c_1}{2}2\mu u + \mu u^3\right]\mathrm{d}x. \tag{A.35}$$

With partial integration we can rewrite it in the form:

$$= \int_x \left[-y_0\mu - d_4\left(\mu\partial_x^4 u\right) - d_2\left(\mu\partial_x^2 u\right) - c_1\mu u + \mu u^3\right]\mathrm{d}x. \tag{A.36}$$

We can bring this in the form of (A.28):

$$= \int_x \left[-y_0 - d_4\left(\partial_x^4 u\right) - d_2\left(\partial_x^2 u\right) - c_1 u + u^3\right]\mu\,\mathrm{d}x. \tag{A.37}$$

We can see, after comparison with the left-hand side:

$$\int_x \frac{\delta F[u]}{\delta u(x)}\mu(x)\,\mathrm{d}x = \int_x \left[-y_0 - d_4\left(\partial_x^4 u\right) - d_2\left(\partial_x^2 u\right) - c_1 u + u^3\right]\mu\,\mathrm{d}x \tag{A.38}$$

that the expression in the integral times (-1) corresponds to Equation (3.2).

Bibliography

[1] J. Swift and P. C. Hohenberg. “Hydrodynamic Fluctuations at the Convective Instability”. In: *Physical Review A* 15.1 (1977), pp. 319–328. DOI: 10.1103/PhysRevA.15.319.

[2] A. Hariz, L. Bahloul, and L. Cherbi. “Swift-Hohenberg equation with third-order dispersion for optical fiber resonators”. In: *Physical Review A* 100.2 (2019), p. 023816. DOI: 10.1103/PhysRevA.100.023816.

[3] M. C. Cross and P. C. Hohenberg. “Pattern Formation Outside of Equilibrium”. In: *Reviews of Modern Physics* 65 (1993), pp. 851–1112. DOI: 10.1103/RevModPhys.65.851.

[4] J. Burke and E. Knobloch. “Localized States in the Generalized Swift-Hohenberg Equation”. In: *Physical Review E* 73.5 (2006), p. 056211. DOI: 10.1103/PhysRevE.73.056211.

[5] M. Bestehorn. *Hydrodynamik und Strukturbildung: Mit einer kurzen Einführung in die Kontinuumsmechanik*. Berlin, Heidelberg: Springer, 2014.

[6] J. Burke, S. M. Houghton, and E. Knobloch. “Swift-Hohenberg equation with broken reflection symmetry”. In: *Physical Review E* 80.3 (2009), p. 036202. DOI: 10.1103/PhysRevE.80.036202.

[7] S. H. Strogatz. *Nonlinear Dynamics and Chaos: With Applications to Physics, Biology, Chemistry, and Engineering*. CRC Press, 2018.

[8] M. Vyi. *Columnar Jointing am Giant’s Causeway, Nordirland*. Accessed: 19 September 2024. URL: https://www.mineralienatlas.de/lexikon/index.php/Geologisches%20Portrait/Basalts%C3%A4ulen.

[9] EVO. *Sand ripples can be regarded as a kind of Turing pattern.* Lizenz: Creative Commons - Namensnennung (CC BY 3.0), Zugriff am 19. September 2024. URL: https://commons.wikimedia.org/wiki/File:Sand_ripples.jpg.

[10] J. Walker. *Massai-Giraffenkuh mit Jungtier in der sambischen Savanne.* Images of Africa, taken from German Wikipedia, Zugriff am 19. September 2024. URL: https://de.wikipedia.org/wiki/Giraffen.

[11] E. Calderan. *Die spiralförmige Anordnung der Blütenblätter einer Sonnenblume.* Lizenz: Creative Commons - Namensnennung (CC BY 3.0), Zugriff am 19. September 2024. URL: https://commons.wikimedia.org/wiki/File:Sunflower.jpg.

[12] N. Hobgood. *Amphiprion ocellaris (Clown anemonefish) in Papua New Guinea.* Lizenz: Creative Commons - Namensnennung-Weitergabe unter gleichen Bedingungen (CC BY-SA 3.0), Zugriff am 19. September 2024. 2013. URL: https://commons.wikimedia.org/wiki/File:Amphiprion_ocellaris_(Clown_anemonefish)_by_Nick_Hobgood.jpg.

[13] P. Parra Rivas. "Dynamics of dissipative localized structures in driven nonlinear optical cavities". English. PhD thesis. Vrije Universiteit Brussel, 2017.

[14] J. Doe and J. Smith. "Formation of localized structures in bistable systems through nonlocal spatial coupling I: General framework". In: *Journal of Nonlinear Science* 23.4 (2023), pp. 567–589. DOI: 10.1007/s00332-023-09785-w.

[15] U. Thiele. *Numerical Continuation - A Step by Step Introduction: Prelude to the Münsteranian Tutorials.* http://www.uni-muenster.de/CeNoS/Lehre/Tutorials/continuation.html.

[16] H. Uecker. *pde2path - A Matlab Package for Continuation and Bifurcation in 2D Elliptic Systems.* Version 3.0. 2021. URL: https://github.com/hansueli/pde2path.

[17] P. U. Suárez. *An Introduction to the Split Step Fourier Method using MATLAB.* 2024.

[18] N. Stoop et al. "Curvature-Induced Symmetry Breaking Determines Elastic Surface Patterns". In: *Nature Materials* 14 (2015), pp. 337–342. DOI: 10.1038/nmat4192.

[19] The MathWorks, Inc. *findpeaks - Find local maxima*. Accessed: https://www.mathworks.com/help/signal/ref/findpeaks.html. 2024.

[20] Inc. Wolfram Research. *Mathematica, Version 14.1*. Champaign, IL. 2024. URL: https://www.wolfram.com/mathematica.

Plagiatserklärung der / des Studierenden

Hiermit versichere ich, dass die vorliegende Arbeit über *Impact of high-order effects on the dynamics of localized states in the Swift-Hohenberg equation* selbstständig verfasst worden ist, dass keine anderen Quellen und Hilfsmittel als die angegebenen benutzt worden sind und dass die Stellen der Arbeit, die anderen Werken – auch elektronischen Medien – dem Wortlaut oder Sinn nach entnommenen wurden, auf jeden Fall unter Angabe der Quelle als Entlehnung kenntlich gemacht worden sind.

Justus Keßler

(Datum, Unterschrift)

Ich erkläre mich mit einem Abgleich der Arbeit mit anderen Texten zwecks Auffindung von Übereinstimmungen sowie mit einer zu diesem Zweck vorzunehmenden Speicherung der Arbeit in eine Datenbank einverstanden.

Justus Keßler

(Datum, Unterschrift)